

Antiferroaxial altermagnetism

Yichen Liu¹ and Cheng-Cheng Liu^{1,*}

¹Centre for Quantum Physics, Key Laboratory of Advanced Optoelectronic Quantum Architecture and Measurement (MOE), School of Physics, Beijing Institute of Technology, Beijing 100081, China

The antiferroaxial state is emerging as an important ferroic order in condensed matter systems. Here, we establish antiferroaxial altermagnetism as a broadly prevalent, generic, and microscopically grounded multiferroic mechanism, in which antiferroaxial counter-rotating distortions both induce altermagnetism and enable its deterministic and reversible switching. Within a unified Landau-theory and symmetry framework, we identify a symmetry-allowed trilinear invariant coupling the antiferroaxial order, the Néel vector, and the altermagnetic order, and derive general symmetry criteria for its occurrence. This coupling locks the induced altermagnetism to the antiferroaxial order, so that reversing the latter reverses the spin splitting and associated time-reversal-odd responses, such as anomalous Hall conductivity. We provide a practical spin group dictionary mapping Néel-vector representations to the resulting d -, g -, and i -wave antiferroaxial altermagnetism, validate the mechanism with ligand-rotation tight-binding models and first-principles calculations, and identify many candidate materials by screening the MAGNDATA and C2DB databases. Our results elevate antiferroaxiality to a universal ferroic control knob for structurally programmable altermagnetic spintronics.

Introduction.— Altermagnetism has attracted widespread attention due to its coexistence of nonrelativistic spin-splitting bands and zero net magnetization, thereby combining key features of ferromagnets and antiferromagnets [1–40]. This unconventional property stems from rotational or mirror symmetries that relate the magnetic sublattices, rather than from translation or inversion symmetries, as illustrated in Fig. 1(a). In the limit of vanishing spin-orbit coupling (SOC), the Néel vector \mathbf{N} of altermagnets transforms as $\Gamma_{\text{AM}} \otimes \Gamma_A^s$, where Γ_{AM} is a nontrivial, inversion-even, one-dimensional (1D) irreducible representation (IR) of the little group at the Γ point, and Γ_A^s denotes the axial-vector IR of the spin-rotation group. The hallmark altermagnetic nonrelativistic spin splitting is characterized by a magnetic multipole $\mathbf{O}^{(\ell)} \equiv \int d^3r [r_{\mu_1} r_{\mu_2} \cdots r_{\mu_\ell}] \mathbf{m}(\mathbf{r})$ with $\mathbf{m}(\mathbf{r})$ the magnetization density and r_μ the Cartesian components [41, 42]. The brackets $[\dots]$ indicate the symmetric-traceless projection over $\mu_1 \cdots \mu_\ell$, so that $\mathbf{O}^{(\ell)}$ transforms as $\Gamma_\ell \otimes \Gamma_A^s$, with Γ_ℓ the rank- ℓ spatial IR. Recent studies have reported that these altermagnetic multipoles can couple to classical multiferroic orders [43–50], such as the ferroelectric and ferroelastic ones, suggesting a path toward altermagnetic multiferroicity.

In addition to conventional ferromagnetic, ferroelectric, and ferroelastic orders, there is a new type of significant ferroic order, the ferroaxial order [51–59]. Ferroaxiality is characterized by the rotational distortion of structural units, represented by the axial vector \mathbf{A} [60], whose magnitude is parameterized by the rotation angle θ . The ferroaxial order transforms according to the axial-vector IR Γ_A and is invariant under inversion and time reversal symmetry. Analogously, the antiferroaxial order is characterized by structural units exhibiting counter-rotating distortions of equal magnitude but op-

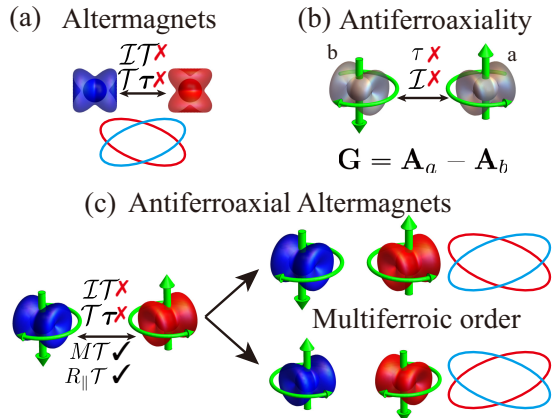


FIG. 1. Antiferroaxial altermagnetism and multiferroic control of the spin splitting. (a) Altermagnet with a spin-splitting isoenergy surface with the red and blue denoting magnetic sublattices; both inversion-time (\mathcal{IT}) and translation-time-reversal ($\mathcal{T}\tau$) symmetries are broken. (b) Antiferroaxiality, characterized by counter-rotating sublattices, is defined as $\mathbf{G} = \mathbf{A}_a - \mathbf{A}_b$ with $\mathbf{A}_{a/b}$ the ferroaxial order on the sublattice a/b . Antiferroaxial order breaks \mathcal{I} and τ that swap the two sublattices, but preserves those acting within each sublattice. (c) In antiferroaxial altermagnets, the coexistence of Néel and antiferroaxial orders breaks \mathcal{IT} and $\mathcal{T}\tau$ while preserving mirror-time (MT) and rotation-time ($R_{\parallel}\mathcal{T}$) symmetries, where \parallel denotes the axis parallel to the antiferroaxial order. Antiferroaxial altermagnetism realizes a broadly prevalent and generic multiferroic mechanism enabling antiferroaxiality-controlled altermagnetic spin splitting.

posite directions along a shared axis [51], as illustrated in Fig. 1(b). This state is characterized by a staggered order parameter $\mathbf{G} = \mathbf{A}_a - \mathbf{A}_b$, where \mathbf{A}_a and \mathbf{A}_b denote the local ferroaxial vectors of sublattices a and b , respectively. Antiferroaxial order commonly occurs in many

systems, such as perovskites and transition metal trifluorides [61–65]. Unlike the ferroelectric order, the ferroaxial and antiferroaxial orders do not require inversion symmetry breaking and can couple to physical quantities such as strain, optical fields, and piezoresistance [56–59].

In this Letter, we propose antiferroaxial altermagnetism, a multiferroic state in which altermagnetism is generated and reversibly switched by the antiferroaxial order. Using symmetry analysis and Landau theory, we demonstrate a symmetry-allowed trilinear coupling among the antiferroaxial order \mathbf{G} , the Néel order \mathbf{N} , and magnetic multipoles $\mathbf{O}^{(\ell)}$, and establish the general symmetry criteria governing this interaction. This coupling dictates that reversing the antiferroaxial order inverts the spin splitting, enabling multiferroic control. Furthermore, Table II classifies the altermagnetic spin point groups and their associated Γ_{AM} , serving as a practical guide for determining the spin splitting type of antiferroaxial altermagnetism. We illustrate antiferroaxial altermagnetism via tight-binding models incorporating ligand rotations, confirming its applicability to generate and control d -, g -, and i -wave altermagnetism. Using first-principles calculations combined with screening the MAGNDATA [66] and C2DB [67, 68] databases, we identify many candidate antiferroaxial altermagnets (Table I). Taking FeF_3 as an example, we demonstrate that reversing the antiferroaxial order not only switches the spin splitting but also inverts the time-reversal-odd responses, such as the anomalous Hall conductivity (AHC), establishing a novel mechanism for structural control of spintronics.

Landau theory.— In Landau theory, an antiferroaxial order \mathbf{G} transforms as $\Gamma_G(\mathbf{q}) \otimes \Gamma_A$ in the parent space group \mathcal{G}_0 , where $\Gamma_G(\mathbf{q})$ is the IR of the little group at the propagation vector \mathbf{q} that encodes the staggered sublattice pattern and Γ_A denotes the axial-vector representation. Similarly, in the zero SOC limit, the Néel vector \mathbf{N} transforms as $\Gamma_N(\mathbf{q}') \otimes \Gamma_A^s$, where $\Gamma_N(\mathbf{q}')$ is the IR of the little group at \mathbf{q}' . A symmetry-allowed trilinear coupling among \mathbf{G} , \mathbf{N} , and $\mathbf{O}^{(\ell)}$ requires that the product of their representations contains the identity representation. Since the spin-rotation sector satisfies $\Gamma_1^s \subset \Gamma_A^s \otimes \Gamma_A^s$, where Γ_1^s is the identity representation in spin-rotation space, the invariance condition reduces to the spatial sector only,

$$\Gamma_1 \subset \Gamma_G(\mathbf{q}) \otimes \Gamma_A \otimes \Gamma_N(\mathbf{q}') \otimes \Gamma_\ell. \quad (1)$$

This implies that the magnetic multipole $\mathbf{O}^{(\ell)}$ can be generally induced by the coexistence of the antiferroaxial order and the Néel vector. Moreover, translational invariance of the coupling enforces momentum conservation, $\mathbf{q}' = -\mathbf{q}$. Equation (1) identifies all symmetry-allowed $\mathbf{O}^{(\ell)}$; specifically, the lowest rank ℓ dictates the type (d -, g -, or i -wave) of the induced altermagnetism. However, the spin-splitting type (planar or bulk) is established only

upon the condensation of \mathbf{G} . Once \mathbf{G} condenses and reduces the symmetry to the isotropy subgroup \mathcal{G} , the Néel vector's representation in \mathcal{G} is obtained by subducing the parent representation, i.e., $\Gamma_N(\mathbf{q}') \downarrow \mathcal{G}$ (see Supplemental Material (SM) [69]). Equation (1) can be stated equivalently as follows: a system is an antiferroaxial altermagnet if and only if, after the antiferroaxial order \mathbf{G} condenses and lowers the symmetry to the isotropy subgroup \mathcal{G} , the subduced representation of the Néel vector, $\Gamma_N(\mathbf{q}') \downarrow \mathcal{G}$, contains a 1D IR that matches one of the Γ_{AM} listed in Table II, which maps each Γ_{AM} to its corresponding splitting type and collinear spin point group.

The coupling dictates that reversing \mathbf{G} at fixed \mathbf{N} necessarily enforces a sign reversal of the magnetic multipole $\mathbf{O}^{(\ell)}$ and the associated spin splitting, thereby establishing the multiferroic mechanism in which a nonmagnetic antiferroaxial order deterministically controls magnetic responses. Unlike ferroelectric orders, the antiferroaxial order does not necessarily break inversion symmetry, allowing this multiferroic control to operate even in nonpolar, centrosymmetric systems.

Model.— To clarify the microscopic mechanism, we perform the explicit symmetry analysis and construct tight-binding models that incorporate the ligand degrees of freedom. This allows us to directly map the antiferroaxial order onto the electronic structure. The model is defined on a lattice with magnetic atoms on sublattices a and b , bridged by nonmagnetic ligands whose rotational distortion encodes the antiferroaxial order [see Fig. 2]. The corresponding Hamiltonian reads (see SM [69])

$$\begin{aligned} \mathcal{H} = & t_M \sum_{\langle mn \rangle} d_m^\dagger d_n + \sum_{mi} [V_{mi}(\theta) d_m^\dagger c_i + \text{h.c.}] \\ & + \sum_{ij} t_{ij}(\theta) c_i^\dagger c_j + J \sum_m \eta_m d_m^\dagger \sigma_z d_m. \end{aligned} \quad (2)$$

Here, d_m^\dagger (c_i^\dagger) denotes the creation operator for an electron on magnetic site m (ligand site i). The first term represents the hopping t_M between nearest-neighbor magnetic sites. The second and third terms describe the magnetic-ligand hybridization $V_{mi}(\theta)$ and the ligand-ligand hopping $t_{ij}(\theta)$, respectively. Crucially, the hopping amplitudes such as $t_{1/2}$ and $V_{1/2}$ vary with the rotation angle θ due to changes in corresponding bond lengths [Figs. 2(a1)-(c1)]. This structural dependence is incorporated via Harrison's scaling law $t(r) \propto r^{-2}$ [70], where the explicit forms of $V_{mi}(\theta)$ and $t_{ij}(\theta)$ are given in SM [69]. The sums over mi and ij run over the symmetry-inequivalent pathways ($V_{1/2}$ and $t_{1/2}$) illustrated in Fig. 2. The final term introduces the local antiferromagnetic exchange J , where σ_z is the spin operator and $\eta_m = \pm 1$ encodes the staggered Néel order.

Figures 2(a1)-(a3) show the geometry, band structure, and spin splitting of the d -wave antiferroaxial altermagnetic model. The antiferroaxial order is parameterized by the ligand rotation angle θ , as illustrated in Fig. 2(a1).

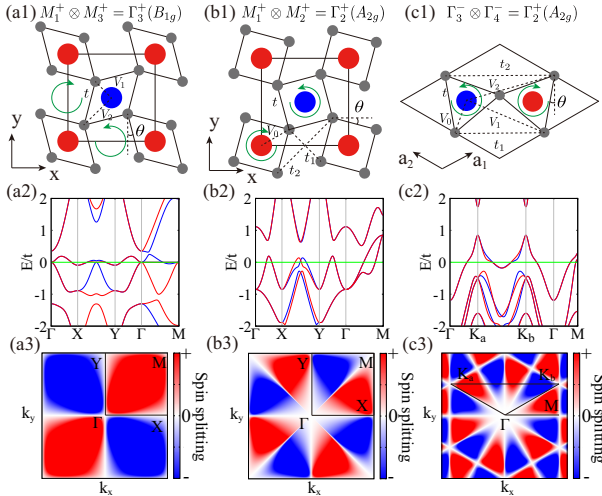


FIG. 2. Antiferroaxial altermagnetism with distinct spin splitting types. Red and blue spheres denote spin-up and spin-down atoms, gray spheres represent ligands, and green arrows indicate rotational distortions. (a)-(c) Illustration of the mechanism (top), band structures (middle), and spin splittings (bottom). (a) d -wave altermagnetism from parent group $P4/mmm$: $N \sim M_1^+$ couples to $G_z \sim M_3^+$ via a $\mathbf{O}^{(2)}$ magnetic multipole in the $\Gamma_3^+(B_{2g})$ channel (Table S1 in SM [69]). Upon symmetry lowering to $P4/mbm$, the Néel vector transforms as $\Gamma_4^+(B_{2g})$, giving a d_{xy} -wave spin splitting in point group $4/mmm$ (Table II). (b) g -wave altermagnetism from parent group $P4/mmm$: $N \sim M_1^+$ couples to $G_z \sim M_2^+$ via the $\Gamma_2^+(A_{2g})$ magnetic multipole channel. In $P4/mbm$, the altermagnetic Néel vector is $\Gamma_2^+(A_{2g})$, corresponding to a planar g -wave spin splitting in $4/mmm$ (Table II). (c) i -wave altermagnetism from parent group $P6/mmm$: $N \sim \Gamma_3^-$ couples to $G_z \sim \Gamma_4^-$ via the $\Gamma_2^+(A_{2g})$ magnetic multipole channel. The symmetry lowering to $\bar{P}6m2$ gives an altermagnetic Néel vector $\Gamma_2(A'_2)$, corresponding to a planar i -wave spin splitting in $\bar{6}m2$ (Table II). The common model parameters are $J = t$ and $t_M = 0.5t$, with specific values: (a) $\theta = 20^\circ$, $V_1 = 1.69t$, $V_2 = 0.37t$; (b) $\theta = 20^\circ$, $V_0 = 1.2t$, $t_1 = 0.7t$, $t_2 = 0.15t$; (c) $\theta = 30^\circ$, $V_0 = 1.2t$, $V_1 = 0.875t$, $V_2 = 0.5t$, $t_1 = 0.6t$, $t_2 = 0.15t$.

The parent phase belongs to space group $P4/mmm$. As a representative scenario, we consider the transitions at the M point, $\mathbf{q} = (\pi, \pi, 0)$, for which $\mathbf{N} \sim M_1^+$ and $\mathbf{G} \sim M_4^+ \otimes (\Gamma_2^+ \oplus \Gamma_5^+)$. For the case in which \mathbf{G} is aligned along the z direction, $G_z \sim M_4^+ \otimes \Gamma_2^+ = M_3^+$. The bilinear combination thus transforms as $\mathbf{N}G_z \sim M_1^+ \otimes M_3^+ = \Gamma_3^+(B_{1g})$, where B_{1g} follows the Mulliken label, while M_i^+ and Γ_i^+ follow the Bradley-Cracknell convention [71]. In the $P4/mmm$ group, the rank-2 multipole representation decomposes as $\mathbf{O}^{(2)} \sim A_{1g} \oplus B_{1g} \oplus B_{2g} \oplus E_g$ (see Table S1 in SM [69]), so the representation constraint in Eq. (1) is satisfied and a symmetry-allowed trilinear invariant exists. When G_z condenses, the system symmetry is reduced to $P4/mbm$ [Fig. 2(a1)], which has crystallographic point group $4/mmm$. The propagation vector \mathbf{q} is folded to the Brillouin-zone center, and the Néel

vector transforms as $\mathbf{N} \sim B_{2g}$ (see details in SM [69]). Table II identifies this IR in point group $4/mmm$ corresponding to a d -wave spin splitting, with the associated altermagnetic spin point group $\bar{4}/\bar{m}\bar{1}mm$. We use Litvin notation for spin point groups here [72]. The numerical results of our generic TB model with $\theta = 20^\circ$ also show the same d -wave spin splitting. Reversing θ , i.e., reversing \mathbf{G} , is symmetry-equivalent to the operation $[E||C_{4z}]$, thereby reversing the sign of the spin splitting (see details in SM [69]). Here $[E||C_{4z}]$ is a spin-group operation, where E denotes the identity operation in spin space and C_{4z} denotes a four-fold rotation in real space.

For the g -wave case, the parent group is also $P4/mmm$. In contrast to Fig. 2(a), here the antiferroaxial order and the Néel order share the same spatial pattern with $\mathbf{N} \sim M_1^+$ and $G_z \sim M_1^+ \otimes \Gamma_2^+ = M_2^+$. The corresponding bilinear combination transforms as $\mathbf{N}G_z \sim M_1^+ \otimes M_2^+ = \Gamma_2^+(A_{2g})$, which cannot couple to $\mathbf{O}^{(2)}$ but can couple to the A_{2g} channel of the $\mathbf{O}^{(4)}$ (see Table S1 in SM [69]). After G_z condenses, the symmetry is reduced to $P4/mbm$ [Fig. 2(b1)] and the Néel vector transforms as $\mathbf{N} \sim A_{2g}$, corresponding to planar g -wave altermagnetism (Table II). The geometry, band structure, and spin splitting are shown in Figs. 2(b1)-(b3), with parameters $\theta = 20^\circ$. Reversing \mathbf{G} is symmetry-equivalent to $[C_2||\tau]$ ($\tau = (1/2, 1/2, 0)$), indicating a spin splitting reversal (see details in SM [69]).

Figures 2(c1)-(c3) show the i -wave antiferroaxial altermagnetic model with parent group $P6/mmm$. Both antiferromagnetic and antiferroaxial transitions occur at the Γ point, transforming as $\mathbf{N} \sim \Gamma_3^-$ and $G_z \sim \Gamma_3^- \otimes \Gamma_4^- = \Gamma_4^-$, respectively. Their coupling yields $\mathbf{N}G_z \sim \Gamma_3^- \otimes \Gamma_4^- = \Gamma_2^+(A_{2g})$, which can couple to $\mathbf{O}^{(6)} \sim 2A_{1g} \oplus A_{2g} \oplus B_{1g} \oplus B_{2g} \oplus 2E_{1g} \oplus 2E_{2g}$ (see Table S1 in SM [69]). After G_z condenses, the space group reduces to $\bar{P}6m2$, and the Néel vector transforms as A'_2 , which identifies the system as a planar i -wave altermagnet (Table II), as shown in Figs. 2 (c2) and (c3) with $\theta = 30^\circ$. Reversing the antiferroaxial order is symmetry-equivalent to $[E||m_{110}]$, which also reverses the spin splitting (see details in SM [69]).

Antiferroaxial altermagnets.— To validate our theoretical framework and demonstrate the ubiquity of the proposed mechanism, we performed a comprehensive screening across the MAGNDATA [66, 73] and C2DB [67, 68] databases. Guided by the above theoretical analysis, we identified a series of candidate materials hosting antiferroaxial altermagnetism, as seen in Table I. In the following, we present two representative examples: the two-dimensional (2D) g -wave altermagnet MnS_2 [74] and the three-dimensional (3D) experimentally synthesized d -wave altermagnet La_2NiO_4 [75], confirming their antiferroaxial altermagnetism via density functional theory (DFT) calculations.

Monolayer MnS_2 [74] is built from $\text{Mn}-\text{S}_4$ tetrahedra possessing S_4 symmetry [Fig. 3(a)]. Its parent phase

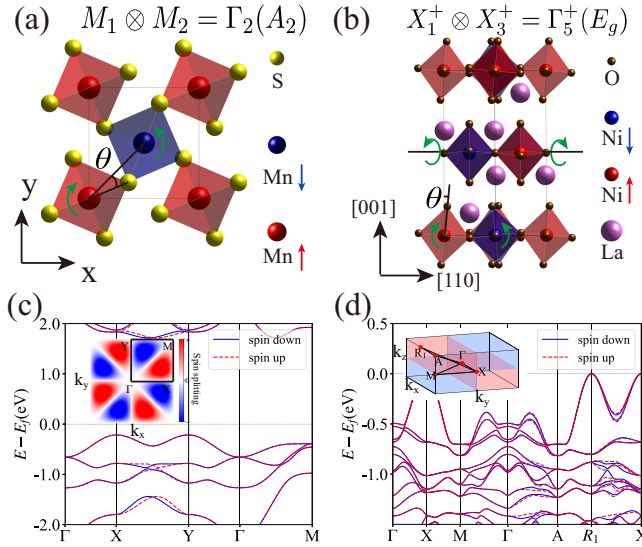


FIG. 3. Antiferroaxial altermagnets. The blue/red spheres and green arrows denote opposite spins and antiferroaxial orders, respectively. (a, c) Monolayer MnS₂ (parent group $P\bar{4}m2$), where Néel (M_1) and antiferroaxial (M_2) orders couple with a $\mathbf{O}^{(4)}$ magnetic multipole in the $\Gamma_2(A_2)$ channel (Table S1 in SM [69]). The symmetry lowers to space group $P\bar{4}2_1m$ with Néel vector $\Gamma_2(A_2)$, corresponding to planar g -wave spin splitting (Table II). (b, d) Bulk La₂NiO₄ (parent group $I4/mmm$), where Néel (X_1^+) and antiferroaxial (X_3^+) orders couple with the $\Gamma_5^+(E_g)$ magnetic multipole channel. The symmetry lowers to space group $Pccn$ with Néel vector $\Gamma_4^+(B_{3g})$, corresponding to d_{yz} -wave splitting (Table II). The insets in the band structures (c, d) illustrate the spin splitting within the Brillouin zone.

belongs to the space group $P\bar{4}m2$. The DFT calculations [74] reveal that both antiferroaxial and antiferromagnetic instabilities emerge at the M point ($\mathbf{q} = (\pi, \pi, 0)$), leading to an ordered state where the Mn-S tetrahedra exhibit a substantial rotational distortion of $\theta \approx 23.4^\circ$. Symmetry analysis indicates that the antiferroaxial and antiferromagnetic order parameters transform according to the irreducible representations $G_z \sim M_2$ and $\mathbf{N} \sim M_1$, respectively. Consequently, $G_z \mathbf{N} \sim M_2 \otimes M_1 = \Gamma_2(A_2)$ can couple to the A_2 channel of the $\mathbf{O}^{(4)}$ (see Table S1 in SM [69]). After G_z condenses, the isotropy subgroup is $P\bar{4}2_1m$ with $\mathbf{N} \sim \Gamma_2(A_2)$, indicating a g -wave spin splitting (Table II), which is corroborated by the DFT results shown in Fig. 3(c).

The 3D Ruddlesden-Popper compound La₂NiO₄ [75] (parent space group $I4/mmm$) consists of corner-sharing Ni-O₆ octahedra [Fig. 3(b)]. Symmetry-mode analysis indicates concomitant antiferroaxial and antiferromagnetic instabilities at the X point [76, 77] ($\mathbf{q} = (\pi, \pi, 0)$), yielding an antiferroaxial rotation pattern with $\theta \approx 6.3^\circ$ together with antiferromagnetic order, i.e., $G_{110} \sim X_3^+$ and $\mathbf{N} \sim X_1^+$. Their bilinear combination transforms as $G_{110} \mathbf{N} \sim X_3^+ \otimes X_1^+ = \Gamma_5^+(E_g)$, which couples to

TABLE I. The candidate antiferroaxial altermagnets and the corresponding altermagnetic types.

spin splitting	antiferroaxial altermagnets
d -wave	La ₂ NiO ₄
planar g -wave	MnA ₂ (A=S,C), KMnF ₃ , Ca ₂ MnO ₄
planar i -wave	FeBr ₃
bulk g -wave	MF ₃ (M=Fe,Co,Ni), LaCrO ₃

the E_g channel of the magnetic multipole $\mathbf{O}^{(2)}$, implying an altermagnetic state. Upon condensation, G_{110} lowers the crystallographic symmetry to $I4_2/ncm$, and the \mathbf{N} further reduces it to space group $Pccn$ with point group mmm . In this state, the Néel order transforms as $\mathbf{N} \sim \Gamma_4^+(B_{3g})$, corresponding to spin point group $\bar{1}mm\bar{1}m$ with d -wave altermagnetism (Table II), confirmed by the band structure calculations [Fig. 3(d)].

Antiferroaxial Multiferroicity.— We formulate the Landau theory in terms of the Landau free energy to demonstrate how the antiferroaxial order switches the spin splitting and the associated physical properties, such as AHC, in altermagnets. As an example, we consider the antiferroaxial multiferroicity in the bulk g -wave altermagnet FeF₃ [63]. FeF₃ is composed of corner-sharing FeF₆ octahedra [Fig. 4(a)]. Starting from the parent space group $Pm\bar{3}m$, it exhibits antiferromagnetic and antiferroaxial instabilities at the R point ($\mathbf{q} = (\pi, \pi, \pi)$). Symmetry analysis gives $\mathbf{G} \sim R_4^+$ and $\mathbf{N} \sim R_1^+$, indicating $\mathbf{GN} \sim R_4^+ \otimes R_1^+ = \Gamma_4^+(T_{1g})$. Since the rank-4 magnetic multipole $\mathbf{O}^{(4)} \sim A_{1g} \oplus E_g \oplus T_{1g} \oplus T_{2g}$ contains a T_{1g} spatial channel (see Table S1 in SM [69]), the representation constraint in Eq. (1) is satisfied, implying a symmetry-allowed trilinear coupling and a g -wave altermagnetism whose planar or bulk character is determined by the orientation of \mathbf{G} .

Based on Landau theory, the free energy can be written as (see the SM [69]):

$$\begin{aligned} \mathcal{F} = & \alpha_N \mathbf{N}^2 + \beta_N (\mathbf{N}^2)^2 + \alpha_G \mathbf{G}^2 + \beta_{G1} (\mathbf{G}^2)^2 \\ & + \beta_{G2} (G_x^2 G_y^2 + G_x^2 G_z^2 + G_y^2 G_z^2) + \mathcal{F}_\epsilon + \mathcal{F}_{\epsilon G} \quad (3) \\ & + \mathcal{F}_O + g \mathbf{N} \cdot (G_x \mathbf{O}_1 + G_y \mathbf{O}_2 + G_z \mathbf{O}_3), \end{aligned}$$

where $\mathbf{O}_1 = \mathbf{O}_{yz(y^2-z^2)}^{(4)}$, $\mathbf{O}_2 = \mathbf{O}_{xz(x^2-z^2)}^{(4)}$, and $\mathbf{O}_3 = \mathbf{O}_{xy(x^2-y^2)}^{(4)}$, with subscripts denoting their spatial symmetries. Here $\mathbf{N}^2 \equiv \mathbf{N} \cdot \mathbf{N}$ and $\mathbf{G}^2 \equiv \mathbf{G} \cdot \mathbf{G}$. The remaining terms \mathcal{F}_O , \mathcal{F}_ϵ , and $\mathcal{F}_{\epsilon G}$ denote the magnetic multipole, elastic, and strain-antiferroaxial coupling contributions, respectively. Eliminating the secondary order parameters by their minimization conditions and substituting the equilibrium values back into \mathcal{F} , we obtain an effective Landau free energy for \mathbf{G} ,

$$\mathcal{F}_{\text{eff}} = \alpha_{\text{eff}} \mathbf{G}^2 + \beta_{1,\text{eff}} (\mathbf{G}^2)^2 + \beta_{2,\text{eff}} (G_x^2 G_y^2 + G_x^2 G_z^2 + G_y^2 G_z^2), \quad (4)$$

where the specific expressions of the effective renormalized coefficients α_{eff} , $\beta_{1,\text{eff}}$ and $\beta_{2,\text{eff}}$ are given in the

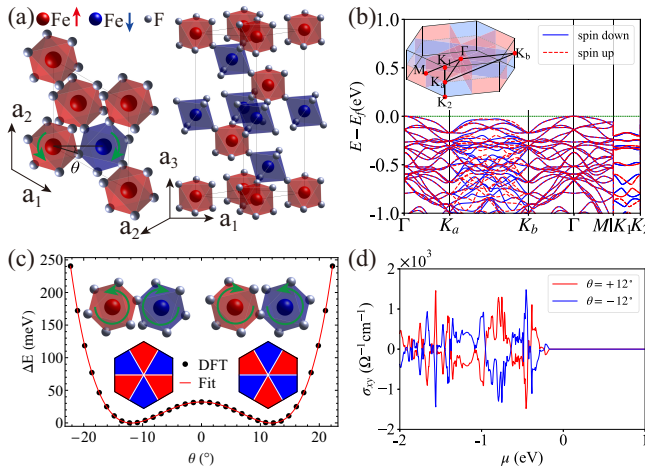


FIG. 4. Multiferroicity with antiferroaxial switchable spin splitting and anomalous Hall conductivity in altermagnets. (a) Top and side views of the crystal structure of FeF₃. Red and blue spheres denote Fe atoms with opposite magnetic moments, while gray spheres represent F atoms. The green curved arrows indicate the antiferroaxial rotation of the Fe-F₆ octahedra, parameterized by the angle θ . (b) Band structure for the lowest-energy configuration at $\theta = 12^\circ$. The inset shows the 3D Brillouin zone with the bulk *g*-wave spin splitting. (c) Total energy as a function of the rotation angle θ , revealing a double-well potential with ground-state minima at $\theta \approx \pm 12^\circ$. The insets illustrate that reversing the structural rotation direction (top) switches the sign of the spin splitting (bottom). The effective Landau free energy is well fit to the model in Eq. 4, yielding $\mathcal{F}_{\text{eff}}(\theta) = 32.1 - 0.446\theta^2 + 1.45 \times 10^{-3}\theta^4$, where θ parameterizes the structural distortion G (in degrees) and \mathcal{F}_{eff} is in meV per unit cell. (d) Anomalous Hall conductivity, calculated as a function of chemical potential at the equilibrium angles $\theta = \pm 12^\circ$, is switchable by antiferroaxial order.

SM [69]. The sign of the anisotropy parameter $\beta_{2,\text{eff}}$ determines the ground state orientation of the antiferroaxial order. When $\beta_{2,\text{eff}} < 0$, the antiferroaxial vector aligns along the (111) direction ($G_x = G_y = G_z$), stabilizing the bulk *g*-wave spin splitting described by $\mathbf{O}^{(4)} \propto (x + y + z)(x - y)(y - z)(z - x)\mathbf{m}(\mathbf{r})$, which is observed in FeF₃ [Fig. 4(b)], NiF₃, CoF₃, and LaCrO₃. Conversely, $\beta_{2,\text{eff}} > 0$ favors alignment along a principal axis (e.g., *x*, *y*, or *z*), leading to a planar *g*-wave splitting, as observed in KMnF₃ and Ca₂MnO₄ [69].

The magnitude of the antiferroaxial order is quantified by the rotation angle θ of the Fe-F₆ octahedra. The DFT calculations reveal a double-well potential for the total energy as a function of θ [Fig. 4(c)], with minima located at $\theta = \pm 12^\circ$. The energy barrier is approximately $\Delta E \approx 30$ meV. Although the Néel vector remains fixed, the two antiferroaxial states ($\pm\theta$) are related by the symmetry operation $[C_2||\boldsymbol{\tau}]$ (where $\boldsymbol{\tau} = (0, 0, 0.5)$) [69]. Consequently, reversing the antiferroaxial order necessitates a reversal of the spin splitting, establishing FeF₃ as an antiferroaxial multiferroic altermagnet. Furthermore,

in the consideration of the SOC, the two antiferroaxial states are related by the $\mathcal{T}\boldsymbol{\tau}$ symmetry. Since the AHC is odd under time-reversal, this symmetry relation dictates that reversing the antiferroaxial order can simultaneously switch the sign of the AHC, and more generally of any time-reversal-odd response, which is confirmed by the calculations shown in Fig. 4(d).

Discussion.— In this Letter, we demonstrate a novel class of multiferroic altermagnetism, termed antiferroaxial altermagnetism, in which altermagnetism is coupled with and tunable by antiferroaxiality. Based on symmetry analysis and Landau theory, we elucidate the general symmetry criteria governing the trilinear coupling between antiferroaxial, antiferromagnetic, and altermagnetic orders. We substantiate this theory by constructing general ligand-rotation tight-binding models for *d*-, *g*-, and *i*-wave antiferroaxial altermagnetism, confirming the coupling between antiferroaxiality and altermagnetism. By screening the MAGNDATA and C2DB databases combined with *ab initio* calculations, we identified a series of material candidates, exemplifying our theory with the 2D *g*-wave altermagnet MnS₂ and the 3D *d*-wave altermagnet La₂NiO₄. Furthermore, using FeF₃ as a prototype, we quantified a switchable energy barrier of 30 meV, demonstrating that reversing the antiferroaxial order deterministically switches the spin splitting and time-reversal-odd responses such as AHC.

Our results establish antiferroaxiality as a key ferroic degree of freedom enabling the emergence and active control of altermagnetism. Recent progress in ferroaxial materials has demonstrated deterministic switching of rotational order using circularly polarized terahertz pulses via nonlinear phonon excitation [56, 57]. Motivated by this progress, and considering that antiferroaxial order arises from staggered rotational lattice modes, the analogous dynamical protocols could be extended to manipulate antiferroaxiality. Importantly, in the present framework, reversing the antiferroaxial order not only flips the altermagnetic spin splitting and associated transport responses, but also constitutes a deterministic reversal of the underlying structural order itself. Furthermore, we show that antiferroaxiality can be efficiently tuned and switched on or off by uniaxial strain, and identify KMnF₃ as a concrete material realization (see SM for details [69]). This work would establish a new paradigm for altermagnetic spintronics, enabling structural-magnetic co-engineering for the active control of spintronic devices even in centrosymmetric materials.

Acknowledgments.— The work is supported by the Science Fund for Creative Research Groups of NSFC (Grant No. 12321004), the NSF of China (Grant No. 12374055), and the National Key R&D Program of China (Grant No. 2020YFA0308800).

* celiu@bit.edu.cn

[1] L. Šmejkal, J. Sinova, and T. Jungwirth, Beyond conventional ferromagnetism and antiferromagnetism: A phase with nonrelativistic spin and crystal rotation symmetry, *Physical Review X* **12**, 031042 (2022).

[2] L. Šmejkal, A. B. Hellenes, R. González-Hernández, J. Sinova, and T. Jungwirth, Giant and tunneling magnetoresistance in unconventional collinear antiferromagnets with nonrelativistic spin-momentum coupling, *Physical Review X* **12**, 011028 (2022).

[3] I. Mazin and The PRX Editors, Editorial: Altermagnetism—a new punch line of fundamental magnetism, *Physical Review X* **12**, 040002 (2022).

[4] C. Wu, K. Sun, E. Fradkin, and S.-C. Zhang, Fermi liquid instabilities in the spin channel, *Physical Review B* **75**, 115103 (2007).

[5] S. Hayami, Y. Yanagi, and H. Kusunose, Momentum-dependent spin splitting by collinear antiferromagnetic ordering, *Journal of the Physical Society of Japan* **88**, 123702 (2019).

[6] L.-D. Yuan, Z. Wang, J.-W. Luo, E. I. Rashba, and A. Zunger, Giant momentum-dependent spin splitting in centrosymmetric low- S_z antiferromagnets, *Physical Review B* **102**, 014422 (2020).

[7] H.-Y. Ma, M. Hu, N. Li, J. Liu, W. Yao, J.-F. Jia, and J. Liu, Multifunctional antiferromagnetic materials with giant piezomagnetism and noncollinear spin current, *Nature Communications* **12**, 2846 (2021).

[8] P. Liu, J. Li, J. Han, X. Wan, and Q. Liu, Spin-group symmetry in magnetic materials with negligible spin-orbit coupling, *Physical Review X* **12**, 021016 (2022).

[9] D.-F. Shao, S.-H. Zhang, M. Li, C.-B. Eom, and E. Y. Tsymbal, Spin-neutral currents for spintronics, *Nature Communications* **12**, 7061 (2021).

[10] Z. Feng, X. Zhou, L. Šmejkal, L. Wu, Z. Zhu, H. Guo, R. González-Hernández, X. Wang, H. Yan, P. Qin, X. Zhang, H. Wu, H. Chen, Z. Meng, L. Liu, Z. Xia, J. Sinova, T. Jungwirth, and Z. Liu, An anomalous hall effect in altermagnetic ruthenium dioxide, *Nature Electronics* **5**, 735 (2022).

[11] H. Bai, Y. C. Zhang, Y. J. Zhou, P. Chen, C. H. Wan, L. Han, W. X. Zhu, S. X. Liang, Y. C. Su, X. F. Han, F. Pan, and C. Song, Efficient spin-to-charge conversion via altermagnetic spin splitting effect in antiferromagnet RuO₂, *Physical Review Letters* **130**, 216701 (2023).

[12] X. Zhou, W. Feng, R.-W. Zhang, L. Šmejkal, J. Sinova, Y. Mokrousov, and Y. Yao, Crystal thermal transport in altermagnetic RuO₂, *Physical Review Letters* **132**, 056701 (2024).

[13] Z. Jin, Z. Zeng, Y. Cao, and P. Yan, Skyrmiion hall effect in altermagnets, *Physical Review Letters* **133**, 196701 (2024).

[14] H.-J. Lin, S.-B. Zhang, H.-Z. Lu, and X. C. Xie, Coulomb drag in altermagnets, *Physical Review Letters* **134**, 136301 (2025).

[15] J. Lai, T. Yu, P. Liu, L. Liu, G. Xing, X.-Q. Chen, and Y. Sun, D -wave flat fermi surface in altermagnets enables maximum charge-to-spin conversion, *Physical Review Letters* **135**, 256702 (2025).

[16] Y.-X. Li and C.-C. Liu, Majorana corner modes and tunable patterns in an altermagnet heterostructure, *Physical Review B* **108**, 205410 (2023).

[17] D. Zhu, Z.-Y. Zhuang, Z. Wu, and Z. Yan, Topological superconductivity in two-dimensional altermagnetic metals, *Physical Review B* **108**, 184505 (2023).

[18] S.-B. Zhang, L.-H. Hu, and T. Neupert, Finite-momentum cooper pairing in proximitized altermagnets, *Nature Communications* **15**, 1801 (2024).

[19] S. A. A. Ghorashi, T. L. Hughes, and J. Cano, Altermagnetic routes to majorana modes in zero net magnetization, *Physical Review Letters* **133**, 106601 (2024).

[20] A. Vijayvargia, E. Day-Roberts, A. S. Botana, and O. Erten, Altermagnets with topological order in kitaev bilayers, *Physical Review Letters* **135**, 166701 (2025).

[21] R. He, D. Wang, N. Luo, J. Zeng, K.-Q. Chen, and L.-M. Tang, Nonrelativistic spin-momentum coupling in antiferromagnetic twisted bilayers, *Physical Review Letters* **130**, 046401 (2023).

[22] B. Pan, P. Zhou, P. Lyu, H. Xiao, X. Yang, and L. Sun, General stacking theory for altermagnetism in bilayer systems, *Physical Review Letters* **133**, 166701 (2024).

[23] Y. Liu, J. Yu, and C.-C. Liu, Twisted magnetic van der waals bilayers: An ideal platform for altermagnetism, *Physical Review Letters* **133**, 206702 (2024).

[24] R.-W. Zhang, C. Cui, R. Li, J. Duan, L. Li, Z.-M. Yu, and Y. Yao, Predictable gate-field control of spin in altermagnets with spin-layer coupling, *Physical Review Letters* **133**, 056401 (2024).

[25] J. Zhou and C. Zhang, Contrasting light-induced spin torque in antiferromagnetic and altermagnetic systems, *Physical Review Letters* **134**, 176902 (2025).

[26] X. Zhu, X. Huo, S. Feng, S.-B. Zhang, S. A. Yang, and H. Guo, Design of altermagnetic models from spin clusters, *Physical Review Letters* **134**, 166701 (2025).

[27] Y. Chen, X. Liu, H.-Z. Lu, and X. C. Xie, Electrical switching of altermagnetism, *Physical Review Letters* **135**, 016701 (2025).

[28] Y. Che, H. Lv, X. Wu, and J. Yang, Engineering altermagnetic states in two-dimensional square tessellations, *Physical Review Letters* **135**, 036701 (2025).

[29] N. Kaushal and M. Franz, Altermagnetism in modified lieb lattice hubbard model, *Physical Review Letters* **135**, 156502 (2025).

[30] V. Leeb, A. Mook, L. Šmejkal, and J. Knolle, Spontaneous formation of altermagnetism from orbital ordering, *Physical Review Letters* **132**, 236701 (2024).

[31] Z.-M. Wang, Y. Zhang, S.-B. Zhang, J.-H. Sun, E. Dagotto, D.-H. Xu, and L.-H. Hu, Spin-orbital altermagnetism, *Physical Review Letters* **135**, 176705 (2025).

[32] J. D. Cao, K. S. Denisov, Y. Liu, and I. Žutić, Symmetry classification for alternating excitons in two-dimensional altermagnets, *Physical Review Letters* **135**, 266703 (2025).

[33] Z.-F. Gao, S. Qu, B. Zeng, Y. Liu, J.-R. Wen, H. Sun, P.-J. Guo, and Z.-Y. Lu, Ai-accelerated discovery of altermagnetic materials, *National Science Review* **12**, nwaf066 (2025).

[34] Q. Cheng and Q.-F. Sun, Orientation-dependent josephson effect in spin-singlet superconductor/altermagnet/spin-triplet superconductor junctions, *Physical Review B* **109**, 024517 (2024).

[35] S.-D. Guo, Y. Liu, J. Yu, and C.-C. Liu, Valley polarization in twisted altermagnetism, *Physical Review B* **110**, L220402 (2024).

[36] S. Zeng and Y.-J. Zhao, Bilayer stacking *a*-type altermagnet: A general approach to generating two-dimensional altermagnetism, *Physical Review B* **110**, 174410 (2024).

[37] M. Ezawa, Third-order and fifth-order nonlinear spin-current generation in $g\pm$ -wave and $i\pm$ -wave altermagnets and perfectly nonreciprocal spin current in $f\pm$ -wave magnets, *Physical Review B* **111**, 125420 (2025).

[38] D. Wang, H. Wang, L. Liu, J. Zhang, and H. Zhang, Electric-field-induced switchable two-dimensional altermagnets, *Nano Letters* **25**, 498 (2025).

[39] Y.-Q. Li, Y.-K. Zhang, X.-L. Lu, Y.-P. Shao, Z.-Q. Bao, J.-D. Zheng, W.-Y. Tong, and C.-G. Duan, Ferrovalley physics in stacked bilayer altermagnetic systems, *Nano Letters* **25**, 6032 (2025).

[40] Z. Song, Z. Qi, C. Fang, Z. Fang, and H. Weng, A unified symmetry classification of magnetic orders via spin space groups: Prediction of coplanar even-wave phases (2025), arXiv:2512.08901 [cond-mat].

[41] P. A. McClarty and J. G. Rau, Landau theory of altermagnetism, *Physical Review Letters* **132**, 176702 (2024).

[42] H. Schiff, P. McClarty, J. G. Rau, and J. Romhányi, Collinear altermagnets and their landau theories, *Physical Review Research* **7**, 033301 (2025).

[43] L. Šmejkal, Altermagnetic multiferroics and altermagnetoelectric effect (2024), arXiv:2411.19928.

[44] W. Sun, W. Wang, C. Yang, R. Hu, S. Yan, S. Huang, and Z. Cheng, Altermagnetism induced by sliding ferroelectricity via lattice symmetry-mediated magnetoelectric coupling, *Nano Letters* **24**, 11179 (2024).

[45] X. Duan, J. Zhang, Z. Zhu, Y. Liu, Z. Zhang, I. Žutić, and T. Zhou, Antiferroelectric altermagnets: Antiferroelectricity alters magnets, *Physical Review Letters* **134**, 106801 (2025).

[46] M. Gu, Y. Liu, H. Zhu, K. Yananose, X. Chen, Y. Hu, A. Stroppa, and Q. Liu, Ferroelectric switchable altermagnetism, *Physical Review Letters* **134**, 106802 (2025).

[47] Y. Zhu, M. Gu, Y. Liu, X. Chen, Y. Li, S. Du, and Q. Liu, Sliding ferroelectric control of unconventional magnetism in stacked bilayers, *Physical Review Letters* **135**, 056801 (2025).

[48] Y. Huang, C. Hua, R. Xu, J. Liu, Y. Zheng, and Y. Lu, Spin inversion enforced by crystal symmetry in ferroelastic altermagnets, *Physical Review Letters* **135**, 266701 (2025).

[49] N. Ding, H. Ye, S.-S. Wang, and S. Dong, Ferroelastically tunable altermagnets, *Physical Review B* **112**, L220410 (2025).

[50] R. Peng, S. Fang, P. Ho, F. Liu, T. Zhou, J. Liu, and Y. S. Ang, Ferroelastic altermagnetism, npj Quantum Materials **10**.1038/s41535-025-00835-7 (2025).

[51] T. Hayashida, K. Kimura, D. Urushihara, T. Asaka, and T. Kimura, Observation of ferrochiral transition induced by an antiferroaxial ordering of antipolar structural units in $\text{Ba}(\text{TiO}_3)\text{Cu}_4(\text{PO}_4)_4$, *Journal of the American Chemical Society* **143**, 3638 (2021).

[52] J. Hlinka, Eight types of symmetrically distinct vectorlike physical quantities, *Physical Review Letters* **113**, 165502 (2014).

[53] R. D. Johnson, L. C. Chapon, D. D. Khalyavin, P. Manuel, P. G. Radaelli, and C. Martin, Giant improper ferroelectricity in the ferroaxial magnet CaMn_7O_2 , *Physical Review Letters* **108**, 067201 (2012).

[54] J. Hlinka, J. Privratska, P. Ondrejkovic, and V. Janovec, Symmetry guide to ferroaxial transitions, *Physical Review Letters* **116**, 177602 (2016).

[55] B. Singh, G. McNamara, K.-M. Kim, S. Siddique, S. D. Funni, W. Zhang, X. Luo, P. Sakrikar, E. M. Kenney, R. Singha, S. Alekseev, S. A. A. Ghorashi, T. J. Hicken, C. Baines, H. Luetkens, Y. Wang, V. M. Plisson, M. Geiwitz, C. A. Occhialini, R. Comin, M. J. Graf, L. Zhao, J. Cano, R. M. Fernandes, J. J. Cha, L. M. Schoop, and K. S. Burch, Ferroaxial density wave from intertwined charge and orbital order in rare-earth tritellurides, *Nature Physics* **21**, 1578 (2025).

[56] Z. Zeng, M. Först, M. Fechner, D. Prabhakaran, P. G. Radaelli, and A. Cavalleri, Photo-induced nonvolatile rewritable ferroaxial switching, *Science* **390**, 195 (2025).

[57] Z. He and G. Khalsa, Optical control of ferroaxial order, *Physical Review Research* **6**, 043220 (2024).

[58] E. Day-Roberts, R. M. Fernandes, and T. Birol, Piezoresistivity as a fingerprint of ferroaxial transitions, *Physical Review Letters* **134**, 016401 (2025).

[59] W. Jin, E. Drueke, S. Li, A. Admasu, R. Owen, M. Day, K. Sun, S.-W. Cheong, and L. Zhao, Observation of a ferro-rotational order coupled with second-order nonlinear optical fields, *Nature Physics* **16**, 42 (2020).

[60] V. M. Dubovik, L. A. Tosunyan, and V. V. Tugushev, Axial toroidal moments in electrodynamics and solid-state physics, *Soviet Journal of Experimental and Theoretical Physics* **63**, 344 (1986).

[61] C. Autret, C. Martin, M. Hervieu, R. Retoux, B. Raveau, G. André, and F. Bourée, Structural investigation of Ca_2MnO_4 by neutron powder diffraction and electron microscopy, *Journal of Solid State Chemistry* **177**, 2044 (2004).

[62] K. S. Knight, D. D. Khalyavin, P. Manuel, C. L. Bull, and P. McIntyre, Nuclear and magnetic structures of Kmnmf_3 perovskite in the temperature interval 10 K–105 K, *Journal of Alloys and Compounds* **842**, 155935 (2020).

[63] S. Lee, S. Torii, Y. Ishikawa, M. Yonemura, T. Moyoshi, and T. Kamiyama, Weak-ferromagnetism of CoF_3 and FeF_3 , *Physica B: Condensed Matter The 11th International Conference on Neutron Scattering (ICNS 2017)*, **551**, 94 (2018).

[64] S. Mattsson and B. Paulus, Density functional theory calculations of structural, electronic, and magnetic properties of the 3d metal trifluorides Mf_3 ($\text{M} = \text{Ti-Ni}$) in the solid state, *Journal of Computational Chemistry* **40**, 1190 (2019).

[65] J. Sødequist and T. Olsen, Two-dimensional altermagnets from high throughput computational screening: Symmetry requirements, chiral magnons, and spin-orbit effects, *Applied Physics Letters* **124**, 182409 (2024).

[66] S. V. Gallego, J. M. Perez-Mato, L. Elcoro, E. S. Tasci, R. M. Hanson, K. Momma, M. I. Aroyo, and G. Madariaga, Magndata: towards a database of magnetic structures. i. the commensurate case, *Applied Crystallography* **49**, 1750 (2016).

[67] M. N. Gjerding, A. Taghizadeh, A. Rasmussen, S. Ali, F. Bertoldo, T. Deilmann, N. R. Knøsgaard, M. Kruse, A. H. Larsen, S. Manti, T. G. Pedersen, U. Petralanda, T. Skovhus, M. K. Svendsen, J. J. Mortensen, T. Olsen, and K. S. Thygesen, Recent progress of the computational 2d materials database (c2db), *2D Materials* **8**, 044002 (2021).

[68] S. Haastrup, M. Strange, M. Pandey, T. Deilmann, P. S. Schmidt, N. F. Hinsche, M. N. Gjerding, D. Torelli, P. M. Larsen, A. C. Riis-Jensen, J. Gath, K. W. Jacobsen,

J. Jørgen Mortensen, T. Olsen, and K. S. Thygesen, The computational 2d materials database: High-throughput modeling and discovery of atomically thin crystals, *2D Materials* **5**, 042002 (2018).

[69] See Supplemental Material for additional details on (I) symmetry-allowed magnetic multipoles in antiferroaxial altermagnets, (II) classification of antiferroaxial altermagnetism, (III) the isotropy subgroup and the subduced representation of the Néel vector, (IV) detailed derivations of the ligand-rotation tight-binding models, (V) symmetry analysis and Landau theory, and (VI) computational details and candidate materials, which includes Refs. [61–65, 70, 74, 75, 78–87].

[70] S. Froyen and W. A. Harrison, Elementary prediction of linear combination of atomic orbitals matrix elements, *Phys. Rev. B* **20**, 2420 (1979).

[71] C. J. Bradley and A. P. Cracknell, *The Mathematical Theory Of Symmetry In Solids: Representation Theory for Point Groups and Space Groups* (Oxford University Press, 2009).

[72] D. B. Litvin, Spin point groups, *Acta Crystallographica Section A* **33**, 279 (1977).

[73] S. V. Gallego, J. M. Perez-Mato, L. Elcoro, E. S. Tasci, R. M. Hanson, M. I. Aroyo, and G. Madariaga, Magnadata: Towards a database of magnetic structures. ii. the incommensurate case, *Journal of Applied Crystallography* **49**, 1941 (2016).

[74] J. Wang, X. Yang, Z. Yang, J. Lu, P. Ho, W. Wang, Y. S. Ang, Z. Cheng, and S. Fang, Pentagonal 2d altermagnets: Material screening and altermagnetic tunneling junction device application, *Advanced Functional Materials* **n/a**, 2505145 (2025).

[75] J. Rodriguez-Carvajal, M. T. Fernandez-Diaz, and J. L. Martinez, Neutron diffraction study on structural and magnetic properties of la2nio4, *Journal of Physics: Condensed Matter* **3**, 3215 (1991).

[76] D. M. Hatch and H. T. Stokes, Complete listing of order parameters for a crystalline phase transition: A solution to the generalized inverse landau problem, *Physical Review B* **65**, 014113 (2001).

[77] H. T. Stokes and D. M. Hatch, Copl: program for obtaining a complete list of order parameters for a group-subgroup crystalline phase transition, *Applied Crystallography* **35**, 379 (2002).

[78] G. Kresse and J. Furthmüller, Efficient iterative schemes for ab initio total-energy calculations using a plane-wave basis set, *Phys. Rev. B* **54**, 11169 (1996).

[79] J. P. Perdew, K. Burke, and M. Ernzerhof, Generalized gradient approximation made simple, *Phys. Rev. Lett.* **77**, 3865 (1996).

[80] A. A. Mostofi, J. R. Yates, Y.-S. Lee, I. Souza, D. Vanderbilt, and N. Marzari, Wannier90: A tool for obtaining maximally-localised wannier functions, *Comput Phys Commun* **178**, 685 (2008).

[81] D. M. Hatch and H. T. Stokes, *Isotropy subgroups of the 230 crystallographic space groups* (World Scientific, 1989).

[82] H. T. Stokes, S. v. Orden, and B. J. Campbell, Isosubgroup: an internet tool for generating isotropy subgroups of crystallographic space groups, *Applied Crystallography* **49**, 1849 (2016).

[83] D. M. Hatch and H. T. Stokes, Invariants: program for obtaining a list of invariant polynomials of the order parameter components associated with irreducible representations of a space group, *Applied Crystallography* **36**, 951 (2003).

[84] M. I. Aroyo, A. Kirov, C. Capillas, J. M. Perez-Mato, and H. Wondratschek, Bilbao Crystallographic Server. II. Representations of crystallographic point groups and space groups, *Acta Crystallographica Section A* **62**, 115 (2006).

[85] J.-S. Zhou, J. A. Alonso, A. Muoñz, M. T. Fernández-Díaz, and J. B. Goodenough, Magnetic Structure of LaCrO₃ Perovskite under High Pressure from In Situ Neutron Diffraction, *Physical Review Letters* **106**, 057201 (2011).

[86] Y. Yao, L. Kleinman, A. H. MacDonald, J. Sinova, T. Jungwirth, D.-s. Wang, E. Wang, and Q. Niu, First principles calculation of anomalous hall conductivity in ferromagnetic bcc fe, *Physical Review Letters* **92**, 037204 (2004).

[87] X. Wang, J. R. Yates, I. Souza, and D. Vanderbilt, Ab initio calculation of the anomalous hall conductivity by wannier interpolation, *Physical Review B* **74**, 195118 (2006).

END MATTER

In the zero SOC limit, a collinear altermagnet is characterized by a Néel vector \mathbf{N} that transforms as $\Gamma_{\text{AM}} \otimes \Gamma_A^s$. Here Γ_{AM} is a nontrivial 1D IR of the crystallographic point group and, when inversion is present, it must be inversion-even, while Γ_A^s denotes the axial vector IR in spin-rotation space. This transformation property implies that neither $\mathcal{T}\tau$ nor \mathcal{IT} enforces spin degeneracy in the zero SOC limit, allowing a momentum-dependent spin splitting. Given the altermagnetic spin point group, we determine whether the ordered phase is altermagnetic and identify whether its spin splitting belongs to the *d*-wave, *g*-wave, or *i*-wave type. In the present work, once the antiferroaxial and Néel orders select a specific Γ_{AM} through the symmetry-allowed coupling, Table II provides a direct lookup of the corresponding spin splitting type. All IRs with allowed nontrivial spin splitting are listed in Table II. A more detailed classification, including the associated lowest-order nodal functions, is provided in Table S3 in SM [69].

It is worth noting that, in the parent group \mathcal{G}_0 , the bilinear product transforms as $\mathbf{G}\mathbf{N} \sim \Gamma_G(\mathbf{q}) \otimes \Gamma_A \otimes \Gamma_N(\mathbf{q}') \otimes \Gamma_A^s$. After \mathbf{G} condenses, the symmetry is lowered to the isotropy subgroup \mathcal{G} , and the order parameter \mathbf{G} transforms as the identity representation, that is $(\Gamma_G(\mathbf{q}) \otimes \Gamma_A) \downarrow \mathcal{G} = \Gamma_1$, and the Néel vector transforms according to the altermagnetic IR $\Gamma_{\text{AM}} \otimes \Gamma_A^s$, namely $(\Gamma_N(\mathbf{q}') \otimes \Gamma_A^s) \downarrow \mathcal{G} = \Gamma_{\text{AM}} \otimes \Gamma_A^s$. Accordingly, Eq. (1) can be stated equivalently as follows: a system realizes antiferroaxial altermagnetism if and only if, upon condensation of the antiferroaxial order, the irreducible representation of the Néel vector in the resulting isotropy subgroup belongs to one of the Γ_{AM} listed in Table II.

TABLE. II. Symmetry classification of antiferroaxial altermagnetism by collinear spin point groups (SPG). The table lists crystallographic point groups (PG) and their symmetry-allowed collinear spin point groups. Γ_{AM} denotes the irreducible representation of the Néel vector. The spin splitting type is categorized into d -wave (d), planar/bulk g -wave ($g_{p/b}$), and planar/bulk i -wave ($i_{p/b}$). The subscripts $\alpha \in \{1, 2, 3\}$ and $\beta \in \{1, 2\}$ denote the distinct irreducible representations corresponding to the same spin point group. Mulliken symbols are used for the irreducible representations of point groups, while spin point groups follow Litvin notation [72]. Groups with no allowed non-trivial spin splitting are omitted.

PG	SPG (Γ_{AM} , Type)	PG	SPG (Γ_{AM} , Type)
2	$\bar{1}2 (B, d)$	32	$3\bar{1}2 (A_2, g_b)$
m	$\bar{1}m (A'', d)$	$3m$	$3\bar{1}m (A_2, g_b)$
$2/m$	$\bar{1}2/\bar{1}m (B_g, d)$	$\bar{3}m$	$\bar{3}\bar{1}m (A_{2g}, g_b)$
222	$2\bar{1}2\bar{1}2 (B_\alpha, d)$	6	$\bar{1}6 (B, g_b)$
$mm2$	$\bar{1}m\bar{1}m2 (A_2, d)$	$\bar{6}$	$\bar{1}\bar{6} (A'', g_b)$
	$m\bar{1}m\bar{1}2 (B_\beta, d)$	$6/m$	$\bar{1}6/\bar{1}m (B_g, g_b)$
mmm	$m\bar{1}m\bar{1}m (B_{\alpha g}, d)$	622	$\bar{1}62\bar{1}2 (B_\beta, g_b)$
4	$\bar{1}4 (B, d)$		$6\bar{1}2\bar{1}2 (A_2, i_p)$
$\bar{4}$	$\bar{1}\bar{4} (B, d)$	$6mm$	$\bar{1}6m\bar{1}m (B_\beta, g_b)$
$4/m$	$\bar{1}4/m (B_g, d)$		$6\bar{1}m\bar{1}m (A_2, i_p)$
422	$\bar{1}42\bar{1}2 (B_\beta, d)$	$\bar{6}m2$	$\bar{1}\bar{6}m\bar{1}2 (A''_2, g_b)$
	$4\bar{1}2\bar{1}2 (A_2, g_p)$		$\bar{1}\bar{6}\bar{1}m2 (A''_2, g_b)$
$4mm$	$\bar{1}4m\bar{1}m (B_\beta, d)$		$\bar{6}\bar{1}m\bar{1}2 (A'_2, i_p)$
	$4\bar{1}m\bar{1}m (A_2, g_p)$	$6/mmm$	$\bar{1}6/\bar{1}mm\bar{1}m (B_{\beta g}, g_b)$
$\bar{4}2m$	$\bar{1}\bar{4}\bar{1}2m (B_2, d)$		$6/m\bar{1}m\bar{1}m (A_{2g}, i_p)$
	$\bar{1}\bar{4}2\bar{1}m (B_1, d)$	$\bar{4}3m$	$\bar{1}\bar{4}3\bar{1}m (A_2, i_b)$
	$\bar{4}\bar{1}2\bar{1}m (A_2, g_p)$	432	$\bar{1}43\bar{1}2 (A_2, i_b)$
$4/mmm$	$\bar{1}4/m\bar{1}mm (B_{\beta g}, d)$	$m\bar{3}m$	$\bar{1}m\bar{3}\bar{1}m (A_{2g}, i_b)$
	$4/m\bar{1}m\bar{1}m (A_{2g}, g_p)$		

Supplementary material for “Antiferroaxial altermagnetism”

Yichen Liu¹ and Cheng-Cheng Liu^{1*}

¹Centre for Quantum Physics, Key Laboratory of Advanced Optoelectronic Quantum Architecture and Measurement (MOE), School of Physics, Beijing Institute of Technology, Beijing 100081, China

This Supplementary Material provides technical details and supporting data for the main text. In Sec. I, we employ symmetry analysis to demonstrate how antiferroaxial order gives rise to d -, g -, and i -wave altermagnetism. Section II classifies antiferroaxial altermagnetism. Section III identifies the isotropy subgroup and derives the subduced representation of the Néel vector. In Sec. IV, we detail the ligand-rotation tight-binding models and present their rigorous derivation, symmetry analysis and band structures. Section V presents a Landau free energy analysis for space group $Pm\bar{3}m$, illustrated by FeF_3 and KMnF_3 . Finally, Sec. VI provides computational details for the density functional theory calculations and candidate antiferroaxial altermagnets, such as MnS_2 , MnC_2 , FeBr_3 , KMnF_3 , Ca_2MnO_4 , FeF_3 , CoF_3 , LaCrO_3 , and La_2NiO_4 .

I. POSSIBLE MAGNETIC MULTipoles IN ANTIFEROAXIAL ALTERMAGNETISM

In this section, we classify the magnetic multipoles induced by coexisting antiferroaxial and Néel orders. This classification determines the symmetry allowed antiferroaxial altermagnetic spin splitting types in each crystallographic point group. We work in the limit of zero spin-orbit coupling (SOC), where the spin and real-space sectors are separable.

In the parent space group \mathcal{G}_0 , an antiferroaxial order parameter \mathbf{G} transforms as $\mathbf{G} \sim \Gamma_G(\mathbf{q}) \otimes \Gamma_A$, where $\Gamma_G(\mathbf{q})$ is an irreducible representation (IR) of the little group at propagation vector \mathbf{q} that encodes the staggered spatial modulation, and Γ_A denotes the axial-vector representation of the crystallographic point group. Similarly, the Néel vector transforms as $\mathbf{N} \sim \Gamma_N(\mathbf{q}') \otimes \Gamma_A^s$, where $\Gamma_N(\mathbf{q}')$ is an IR of the little group at \mathbf{q}' and Γ_A^s is the axial-vector representation in spin-rotation space.

The nonrelativistic spin splitting in altermagnets can be parameterized by magnetic multipoles, defined as rank- ℓ symmetric-traceless moments of the magnetization density $\mathbf{m}(\mathbf{r})$,

$$\mathbf{O}^{(\ell)} \equiv \int d^3r [r_{\mu_1} r_{\mu_2} \cdots r_{\mu_\ell}] \mathbf{m}(\mathbf{r}), \quad (\text{S-1})$$

where r_μ are Cartesian components of \mathbf{r} and $[\dots]$ denotes the symmetric-traceless projection over $\mu_1 \cdots \mu_\ell$. By construction, $\mathbf{O}^{(\ell)}$ transforms as $\Gamma_\ell \otimes \Gamma_A^s$, where Γ_ℓ is the spatial rank- ℓ representation (dimension $2\ell + 1$) that subduces into IRs of the crystallographic point group. The ranks $\ell = 2, 4, 6$ correspond to the d -, g -, and i -wave altermagnetic symmetries, respectively.

We consider a symmetry-allowed trilinear invariant coupling among \mathbf{G} , \mathbf{N} , and $\mathbf{O}^{(\ell)}$. In the parent phase, the identity representation must preserve the translational symmetry of the parent group, which enforces momentum conservation, $\mathbf{q} + \mathbf{q}' = \mathbf{K}$ (where \mathbf{K} is a reciprocal lattice vector); i.e., $\mathbf{q}' = -\mathbf{q}$ up to a reciprocal lattice vector. Since $\Gamma_1^s \subset \Gamma_A^s \otimes \Gamma_A^s$, the invariance condition reduces to the real-space sector

$$\Gamma_1 \subset \Gamma_G(\mathbf{q}) \otimes \Gamma_A \otimes \Gamma_N(\mathbf{q}') \otimes \Gamma_\ell. \quad (\text{S-2})$$

Hereafter, we suppress the spin-rotation factor Γ_A^s for notational brevity. It is convenient to introduce the combined modulation representation $\Gamma_0 \equiv \Gamma_G(\mathbf{q}) \otimes \Gamma_N(\mathbf{q}')$, so that the bilinear coupling transforms as $\mathbf{N}\mathbf{G} \sim \Gamma_0 \otimes \Gamma_A$. Equation (S-2) then reduces to a purely spatial selection rule: a trilinear invariant exists if and only if $\Gamma_0 \otimes \Gamma_A$ and the multipole sector Γ_ℓ share at least one common point-group IR, i.e.,

$$(\Gamma_0 \otimes \Gamma_A) \cap \Gamma_\ell \neq \emptyset. \quad (\text{S-3})$$

Therefore, once $\Gamma_G(\mathbf{q})$ and $\Gamma_N(\mathbf{q}')$ are specified in the parent group, this criterion fixes the lowest allowed multipole rank ℓ_{\min} (and hence the $d/g/i$ -wave class), while the detailed basis form (e.g., d_{xy} versus $d_{x^2-y^2}$) is only resolved after the order parameter condenses and the system reduces to the isotropy subgroup.

* ccliu@bit.edu.cn

TABLE S1. Decomposition of magnetic multipoles under crystallographic point groups. The table lists the irreducible representations (IRs) contained in the spatial sector Γ_ℓ of the magnetic multipoles for rank $\ell = 2$ (*d*-wave altermagnetism), $\ell = 4$ (*g*-wave altermagnetism), and $\ell = 6$ (*i*-wave altermagnetism). The notation follows the Mulliken symbols.

Point Group	<i>d</i> -wave ($\ell = 2$)	<i>g</i> -wave ($\ell = 4$)	<i>i</i> -wave ($\ell = 6$)
$\bar{1}$	$5A_u$	$9A_u$	$13A_u$
2	$3A \oplus 2B$	$5A \oplus 4B$	$7A \oplus 6B$
m	$3A' \oplus 2A''$	$5A' \oplus 4A''$	$7A' \oplus 6A''$
$2/m$	$3A_g \oplus 2B_g$	$5A_g \oplus 4B_g$	$7A_g \oplus 6B_g$
222	$2A \oplus B_1 \oplus B_2 \oplus B_3$	$3A \oplus 2B_1 \oplus 2B_2 \oplus 2B_3$	$4A \oplus 3B_1 \oplus 3B_2 \oplus 3B_3$
mm2	$2A_1 \oplus A_2 \oplus B_1 \oplus B_2$	$3A_1 \oplus 2A_2 \oplus 2B_1 \oplus 2B_2$	$4A_1 \oplus 3A_2 \oplus 3B_1 \oplus 3B_2$
mmm	$2A_g \oplus B_{1g} \oplus B_{2g} \oplus B_{3g}$	$3A_g \oplus 2B_{1g} \oplus 2B_{2g} \oplus 2B_{3g}$	$4A_g \oplus 3B_{1g} \oplus 3B_{2g} \oplus 3B_{3g}$
$4, \bar{4}$	$A \oplus 2B \oplus E$	$3A \oplus 2B \oplus 2E$	$3A \oplus 4B \oplus 3E$
$4/m$	$A_g \oplus 2B_g \oplus E_g$	$3A_g \oplus 2B_g \oplus 2E_g$	$3A_g \oplus 4B_g \oplus 3E_g$
422, 4mm, $\bar{4}2m$	$A_1 \oplus B_1 \oplus B_2 \oplus E$	$2A_1 \oplus A_2 \oplus B_1 \oplus B_2 \oplus 2E$	$2A_1 \oplus A_2 \oplus 2B_1 \oplus 2B_2 \oplus 3E$
$4/mmm$	$A_{1g} \oplus B_{1g} \oplus B_{2g} \oplus E_g$	$2A_{1g} \oplus A_{2g} \oplus B_{1g} \oplus B_{2g} \oplus 2E_g$	$2A_{1g} \oplus A_{2g} \oplus 2B_{1g} \oplus 2B_{2g} \oplus 3E_g$
3	$2E$	$3E$	$4E$
$\bar{3}$	$A_g \oplus 2E_g$	$3A_g \oplus 3E_g$	$5A_g \oplus 4E_g$
32, 3m	$A_1 \oplus 2E$	$2A_1 \oplus A_2 \oplus 3E$	$3A_1 \oplus 2A_2 \oplus 4E$
$\bar{3}m$	$A_{1g} \oplus 2E_g$	$2A_{1g} \oplus A_{2g} \oplus 3E_g$	$3A_{1g} \oplus 2A_{2g} \oplus 4E_g$
6	$A \oplus E_1 \oplus E_2$	$A \oplus 2B \oplus E_1 \oplus 2E_2$	$3A \oplus 2B \oplus 2E_1 \oplus 2E_2$
$\bar{6}$	$A' \oplus E' \oplus E''$	$2A' \oplus A'' \oplus 2E' \oplus E''$	$3A' \oplus 2A'' \oplus 2E' \oplus 2E''$
$6/m$	$A_g \oplus E_{1g} \oplus E_{2g}$	$A_g \oplus 2B_g \oplus E_{1g} \oplus 2E_{2g}$	$3A_g \oplus 2B_g \oplus 2E_{1g} \oplus 2E_{2g}$
622, 6mm	$A_1 \oplus E_1 \oplus E_2$	$A_1 \oplus B_1 \oplus B_2 \oplus E_1 \oplus 2E_2$	$2A_1 \oplus A_2 \oplus B_1 \oplus B_2 \oplus E_1 \oplus 2E_2$
$\bar{6}m2$	$A'_1 \oplus E' \oplus E''$	$A'_1 \oplus A'_1 \oplus A''_2 \oplus E'' \oplus 2E'$	$2A'_1 \oplus A'_2 \oplus A'_1 \oplus A''_2 \oplus 2E' \oplus 2E''$
$6/mmm$	$A_{1g} \oplus E_{1g} \oplus E_{2g}$	$A_{1g} \oplus B_{1g} \oplus B_{2g} \oplus E_{1g} \oplus 2E_{2g}$	$2A_{1g} \oplus A_{2g} \oplus B_{1g} \oplus B_{2g} \oplus 2E_{1g} \oplus 2E_{2g}$
23	$E \oplus T$	$A \oplus E \oplus 2T$	$2A \oplus E \oplus 2T$
$m\bar{3}$	$E_g \oplus T_g$	$A_g \oplus E_g \oplus 2T_g$	$2A_g \oplus E_g \oplus 3T_g$
432, $\bar{4}3m$	$E \oplus T_2$	$A_1 \oplus E \oplus T_1 \oplus T_2$	$A_1 \oplus A_2 \oplus E \oplus T_1 \oplus 2T_2$
$m\bar{3}m$	$E_g \oplus T_{2g}$	$A_{1g} \oplus E_g \oplus T_{1g} \oplus T_{2g}$	$A_{1g} \oplus A_{2g} \oplus E_g \oplus T_{1g} \oplus 2T_{2g}$

In practice, for each crystallographic point group, we: (i) specify the real-space axial-vector representation Γ_A ; (ii) enumerate admissible Γ_0 compatible with a collinear Néel order in that point group (for centrosymmetric groups, Γ_0 must be inversion-even for the even- ℓ multipoles considered here); (iii) tabulate $\Gamma_0 \otimes \Gamma_A$; and (iv) determine the lowest $\ell = 2, 4, 6$ whose multipole decomposition contains at least one IR that also appears in the decomposition of $\Gamma_0 \otimes \Gamma_A$. The decompositions of Γ_ℓ into point-group IRs are listed in Table S1, and the resulting allowed spin-splitting types are summarized in Table S2.

This analysis shows that antiferroaxiality generically enables *d*-, *g*-, and *i*-wave altermagnetic spin splitting depending on the point-group symmetry and the specific Γ_0 channel selected by the antiferroaxial–Néel coexistence.

II. CLASSIFICATION OF ANTIFERROAXIAL ALTERMAGNETISM IN TERMS OF SPIN POINT GROUP

In the zero SOC limit, the altermagnetism is captured in Landau theory by requiring that the Néel vector transforms as $\mathbf{N} \sim \Gamma_{\text{AM}} \otimes \Gamma_A^s$, where Γ_{AM} is a nontrivial, inversion-even, one-dimensional irreducible representation (IR) of the crystallographic point group, and Γ_A^s denotes the axial-vector IR in spin-rotation space. The nonrelativistic spin splitting is conveniently characterized by a magnetic multipole, $\mathbf{O}^{(\ell)} \sim \Gamma_\ell \otimes \Gamma_A^s$, which appears as a secondary order parameter linearly coupled to altermagnetic Néel vector \mathbf{N} . Accordingly, the type of altermagnetism is determined by the lowest-rank multipole sector (smallest ℓ) that is symmetry-allowed to couple to the Néel order, with $\ell = 2, 4, 6$ corresponding to the *d*-, *g*-, and *i*-wave altermagnetism, respectively. Table S3 provides a comprehensive classification of these symmetry-allowed antiferroaxial altermagnetic phases, listing the corresponding spin point groups, irreducible representations, and lowest-order nodal functions for all relevant crystallographic point groups.

TABLE S2. Symmetry criteria for antiferroaxial altermagnetism. The table lists the axial vector representation Γ_A and the product representation $\Gamma_0 \otimes \Gamma_A$ for each point group. Γ_0 is an inversion-even IR representing the combined spatial parity of the antiferroaxial and Néel orders. The last column indicates the allowed altermagnetic spin splitting types (d -, g -, or i -wave) derived from the overlap with Table S1.

Point Group	Γ_A	Possible $\Gamma_0 \otimes \Gamma_A$	Allowed Spin Splitting
$\bar{1}$	$3A_g$	$3A_g$	\emptyset
2	$A \oplus 2B$	$A \oplus 2B, B \oplus 2A$	d
m	$A' \oplus 2A''$	$A' \oplus 2A'', A'' \oplus 2A'$	d
$2/m$	$A_g \oplus 2B_g$	$A_g \oplus 2B_g, B_g \oplus 2A_g$	d
222	$B_1 \oplus B_2 \oplus B_3$	$B_1 \oplus B_2 \oplus B_3, A \oplus B_2 \oplus B_3, A \oplus B_1 \oplus B_3, A \oplus B_1 \oplus B_2$	d
mm2	$A_2 \oplus B_1 \oplus B_2$	$A_2 \oplus B_1 \oplus B_2, A_1 \oplus B_1 \oplus B_2, A_1 \oplus A_2 \oplus B_2, A_1 \oplus A_2 \oplus B_1$	d
mmm	$B_{1g} \oplus B_{2g} \oplus B_{3g}$	$B_{1g} \oplus B_{2g} \oplus B_{3g}, A_g \oplus B_{2g} \oplus B_{3g}, A_g \oplus B_{1g} \oplus B_{3g}$	d
4	$A \oplus E$	$A \oplus E, B \oplus E, 2A \oplus 2B \oplus E$	d
$\bar{4}$	$A \oplus E$	$A \oplus E, B \oplus E, 2A \oplus 2B \oplus E$	d
$4/m$	$A_g \oplus E_g$	$A_g \oplus E_g, B_g \oplus E_g, 2A_g \oplus 2B_g \oplus E_g$	d
422	$A_2 \oplus E$	$A_2 \oplus E, A_1 \oplus E, B_2 \oplus E, B_1 \oplus E,$ $A_1 \oplus A_2 \oplus B_1 \oplus B_2 \oplus E$	d, g
4mm	$A_2 \oplus E$	$A_2 \oplus E, A_1 \oplus E, B_2 \oplus E, B_1 \oplus E,$ $A_1 \oplus A_2 \oplus B_1 \oplus B_2 \oplus E$	d, g
$\bar{4}2m$	$A_2 \oplus E$	$A_2 \oplus E, A_1 \oplus E, B_1 \oplus E, B_2 \oplus E,$ $A_1 \oplus A_2 \oplus B_1 \oplus B_2 \oplus E$	d, g
4/mmm	$A_{2g} \oplus E_g$	$A_{2g} \oplus E_g, A_{1g} \oplus E_g, B_{1g} \oplus E_g, B_{2g} \oplus E_g,$ $A_{1g} \oplus A_{2g} \oplus B_{1g} \oplus B_{2g} \oplus E_g$ $A \oplus E, 2A \oplus 2E$	d, g
3	$A \oplus E$	$A \oplus E, 2A \oplus 2E$	d
$\bar{3}$	$A_g \oplus E_g$	$A_g \oplus E_g, 2A_g \oplus 2E_g$	d
32	$A_2 \oplus E$	$A_2 \oplus E, A_1 \oplus E, A_1 \oplus A_2 \oplus 2E$	d, g
3m	$A_2 \oplus E$	$A_2 \oplus E, A_1 \oplus E, A_1 \oplus A_2 \oplus 2E$	d, g
$\bar{3}m$	$A_{2g} \oplus E_g$	$A_{2g} \oplus E_g, A_{1g} \oplus E_g, A_{1g} \oplus A_{2g} \oplus 2E_g$	d, g
6	$A \oplus E_1$	$A \oplus E_1, B \oplus E_2, 2A \oplus E_1 \oplus E_2, 2B \oplus E_1 \oplus E_2$	d, g
$\bar{6}$	$A' \oplus E'$	$A' \oplus E', A'' \oplus E'', 2A' \oplus 2E', 2A'' \oplus 2E''$	d, g
$6/m$	$A_g \oplus E_{1g}$	$A_g \oplus E_{1g}, B_g \oplus E_{2g}, 2A_g \oplus E_{1g} \oplus E_{2g}, 2B_g \oplus E_{1g} \oplus E_{2g}$	d, g
622	$A_2 \oplus E_1$	$A_2 \oplus E_1, A_1 \oplus E_1, B_2 \oplus E_2, B_1 \oplus E_2,$ $A_1 \oplus A_2 \oplus E_1 \oplus E_2, B_1 \oplus B_2 \oplus E_1 \oplus E_2$	d, g, i
6mm	$A_2 \oplus E_1$	$A_2 \oplus E_1, A_1 \oplus E_1, B_2 \oplus E_2, B_1 \oplus E_2,$ $A_1 \oplus A_2 \oplus E_1 \oplus E_2, B_1 \oplus B_2 \oplus E_1 \oplus E_2$	d, g, i
$\bar{6}m2$	$A'_2 \oplus E''$	$A'_2 \oplus E'', A'_1 \oplus E'', A''_2 \oplus E', A''_1 \oplus E',$ $A'_1 \oplus A''_2 \oplus E' \oplus E'', A'_1 \oplus A'_2 \oplus E' \oplus E''$	d, g, i
6/mmm	$A_{2g} \oplus E_{1g}$	$A_{2g} \oplus E_{1g}, A_{1g} \oplus E_{1g}, B_{2g} \oplus E_{2g}, B_{1g} \oplus E_{2g},$ $A_{1g} \oplus A_{2g} \oplus E_{1g} \oplus E_{2g}, B_{1g} \oplus B_{2g} \oplus E_{1g} \oplus E_{2g}$	d, g, i
23	T	$T, 2T, A \oplus E \oplus 2T$	d
$m\bar{3}$	T_g	$T_g, 2T_g, A_g \oplus E_g \oplus 2T_g$	d
432	T_1	$T_1, T_2, T_1 \oplus T_2,$ $A_2 \oplus E \oplus T_1 \oplus T_2, A_1 \oplus E \oplus T_1 \oplus T_2$	d, g, i
$\bar{4}3m$	T_1	$T_1, T_2, T_1 \oplus T_2,$ $A_2 \oplus E \oplus T_1 \oplus T_2, A_1 \oplus E \oplus T_1 \oplus T_2$	d, g, i
$m\bar{3}m$	T_{1g}	$T_{1g}, T_{2g}, T_{1g} \oplus T_{2g},$ $A_{1g} \oplus E_G \oplus T_{1g} \oplus T_{2g}, A_{2g} \oplus E_G \oplus T_{1g} \oplus T_{2g}$	d, g, i

III. ISOTROPY SUBGROUP AND IRREP SUBDUCTION

The isotropy subgroup \mathcal{G} [1] associated with the condensation of the antiferroaxial order parameter is determined by the parent space group \mathcal{G}_0 , the parent irrep, and the chosen order parameter direction. For the selected order parameter direction, the corresponding subgroup setting provides the basis transformation and, when applicable, the origin shift. These relations define the supercell in the low symmetry setting and thereby determine how the relevant propagation vector is folded to the Γ point when expressed in the reciprocal basis of \mathcal{G} .

TABLE S3. Classification of antiferroaxial altermagnetism. This table lists only the symmetry-allowed altermagnetic orders, excluding ferromagnetic (FM) and trivial non-splitting cases. It provides the point group (PG), the specific collinear spin point group (SPG) notation reflecting the preserved spatial axes, the corresponding irreducible representation (Γ_{AM}), and the spin splitting type with the lowest-order nodal function.

PG	SPG (Γ_{AM})	Splitting [Function]	PG	SPG (Γ_{AM})	Splitting [Function]
2	$\bar{1}2 (B)$	<i>d</i> -wave [xy]	$4/mmm$	$4/m^1m\bar{1}m (A_{2g})$	<i>g</i> -wave [$xy(x^2 - y^2)$]
m	$\bar{1}m (A'')$	<i>d</i> -wave [xy]		$\bar{1}4/mm\bar{1}m (B_{1g})$	<i>d</i> -wave [$x^2 - y^2$]
$2/m$	$\bar{1}2/\bar{1}m (B_g)$	<i>d</i> -wave [xy]		$\bar{1}4/m\bar{1}mm (B_{2g})$	<i>d</i> -wave [xy]
222	$\bar{1}2\bar{1}22 (B_1)$	<i>d</i> -wave [xy]	32	$3\bar{1}2 (A_2)$	<i>g</i> -wave [$z(x^3 - 3xy^2)$]
	$\bar{1}2\bar{2}\bar{1}2 (B_2)$	<i>d</i> -wave [xz]	3m	$3\bar{1}m (A_2)$	<i>g</i> -wave [$z(x^3 - 3xy^2)$]
	$2\bar{1}2\bar{1}2 (B_3)$	<i>d</i> -wave [yz]	$\bar{3}m$	$\bar{3}\bar{1}m (A_{2g})$	<i>g</i> -wave [$z(x^3 - 3xy^2)$]
$mm2$	$\bar{1}m\bar{1}m2 (A_2)$	<i>d</i> -wave [xy]	6	$\bar{1}6 (B)$	<i>g</i> -wave [$z(x^3 - 3xy^2)$]
	$m\bar{1}m\bar{1}2 (B_1)$	<i>d</i> -wave [xz]	$\bar{6}$	$\bar{1}\bar{6} (A'')$	<i>g</i> -wave [$z(x^3 - 3xy^2)$]
	$\bar{1}mm\bar{1}2 (B_2)$	<i>d</i> -wave [yz]	$6/m$	$\bar{1}6/\bar{1}m (B_g)$	<i>g</i> -wave [$z(x^3 - 3xy^2)$]
mmm	$\bar{1}m\bar{1}mm (B_{1g})$	<i>d</i> -wave [xy]	622	$6\bar{1}2\bar{1}2 (A_2)$	<i>i</i> -wave [$xy(3x^2 - y^2)(x^2 - 3y^2)$]
	$\bar{1}mm\bar{1}m (B_{2g})$	<i>d</i> -wave [xz]		$\bar{1}62\bar{1}2 (B_1)$	<i>g</i> -wave [$z(3x^2y - y^3)$]
	$m\bar{1}m\bar{1}m (B_{3g})$	<i>d</i> -wave [yz]		$\bar{1}6\bar{1}22 (B_2)$	<i>g</i> -wave [$z(x^3 - 3xy^2)$]
4	$\bar{1}4 (B)$	<i>d</i> -wave [$x^2 - y^2, xy$]	$6mm$	$6\bar{1}m\bar{1}m (A_2)$	<i>i</i> -wave [$xy(3x^2 - y^2)(x^2 - 3y^2)$]
$\bar{4}$	$\bar{1}\bar{4} (B)$	<i>d</i> -wave [$x^2 - y^2, xy$]		$\bar{1}6m\bar{1}m (B_1)$	<i>g</i> -wave [$z(3x^2y - y^3)$]
$4/m$	$\bar{1}4/m (B_g)$	<i>d</i> -wave [$x^2 - y^2, xy$]		$\bar{1}6\bar{1}mm (B_2)$	<i>g</i> -wave [$z(x^3 - 3xy^2)$]
422	$4\bar{1}2\bar{1}2 (A_2)$	<i>g</i> -wave [$xy(x^2 - y^2)$]	6m2	$6\bar{1}m\bar{1}2 (A_2')$	<i>i</i> -wave [$xy(3x^2 - y^2)(x^2 - 3y^2)$]
	$\bar{1}42\bar{1}2 (B_1)$	<i>d</i> -wave [$x^2 - y^2$]		$\bar{1}6\bar{1}m2 (A_1'')$	<i>g</i> -wave [$z(3x^2y - y^3)$]
	$\bar{1}4\bar{1}22 (B_2)$	<i>d</i> -wave [xy]		$\bar{1}6m\bar{1}2 (A_2'')$	<i>g</i> -wave [$z(x^3 - 3xy^2)$]
4mm	$4\bar{1}m\bar{1}m (A_2)$	<i>g</i> -wave [$xy(x^2 - y^2)$]	$6/mmm$	$6/m^1m\bar{1}m (A_{2g})$	<i>i</i> -wave [$xy(3x^2 - y^2)(x^2 - 3y^2)$]
	$\bar{1}4m\bar{1}m (B_1)$	<i>d</i> -wave [$x^2 - y^2$]		$\bar{1}6/mm\bar{1}m (B_{1g})$	<i>g</i> -wave [$z(3x^2y - y^3)$]
	$\bar{1}4\bar{1}mm (B_2)$	<i>d</i> -wave [xy]		$\bar{1}6/m\bar{1}mm (B_{2g})$	<i>g</i> -wave [$z(x^3 - 3xy^2)$]
$\bar{4}2m$	$\bar{4}\bar{1}2\bar{1}m (A_2)$	<i>g</i> -wave [$xy(x^2 - y^2)$]	432	$\bar{1}43\bar{1}2 (A_2)$	<i>i</i> -wave [$(x^2 - y^2)(y^2 - z^2)(z^2 - x^2)$]
	$\bar{1}42\bar{1}m (B_1)$	<i>d</i> -wave [$x^2 - y^2$]	43m	$\bar{1}43\bar{1}m (A_2)$	<i>i</i> -wave [$(x^2 - y^2)(y^2 - z^2)(z^2 - x^2)$]
	$\bar{1}4\bar{1}2m (B_2)$	<i>d</i> -wave [xy]	$m\bar{3}m$	$\bar{1}4/m\bar{3}\bar{1}2/\bar{1}m (A_{2g})$	<i>i</i> -wave [$(x^2 - y^2)(y^2 - z^2)(z^2 - x^2)$]

To determine the real space representation of the Néel order in the isotropy subgroup, we subduce the parent representation to \mathcal{G} , $\Gamma_N^{\mathcal{G}} = \Gamma_N(\mathbf{q}') \downarrow \mathcal{G}$, with \mathbf{q}' mapped to the folded Γ point by the above supercell relation. In practice, the subduction and the identification of the resulting irreps in \mathcal{G} can be carried out using the representation tools hosted by the Bilbao Crystallographic Server [2], which implement the required correlation and compatibility analysis between the parent group and the subgroup.

IV. LIGAND-ROTATION TIGHT-BINDING MODELS

In this section, we provide a detailed derivation of the tight-binding (TB) models for the *d*-, *g*-, and *i*-wave antiferroaxial altermagnets introduced in the main text. These models explicitly incorporate the ligand degrees of freedom to elucidate the microscopic origin of the nonrelativistic spin splitting. The axial-vector IR within the spin-rotation space, denoted Γ_A^s , are omitted here and throughout the subsequent analysis.

The TB Hamiltonian can be written as

$$\mathcal{H} = t_M \sum_{\langle mn \rangle} d_m^\dagger d_n + \sum_{mi} \left[V_{mi}(\theta) d_m^\dagger c_i + \text{h.c.} \right] + \sum_{ij} t_{ij}(\theta) c_i^\dagger c_j + J \sum_m \eta_m d_m^\dagger \sigma_z d_m, \quad (\text{S-4})$$

where d_m^\dagger (c_i^\dagger) creates an electron on the magnetic (ligand) site, and $\eta_m = \pm 1$ encodes the staggered Néel order. The first term describes the direct nearest-neighbor hopping between magnetic sites with amplitude t_M . The second and third terms describe the magnetic-ligand hybridization $V_{mi}(\theta)$ and ligand-ligand hopping $t_{ij}(\theta)$, respectively, both controlled by the antiferroaxial rotation angle θ through the bond-length dependence of hopping integrals [e.g., $V_{1,2}$ and $t_{1,2}$ in Fig. S1(a2)-(c2)]. Following the main text, we incorporate this structural dependence via Harrison's scaling law $t(r) \propto r(\theta)^{-2}$ [3]. The last term introduces a local exchange field of strength J , with σ_z the Pauli matrix and the quantization axis chosen along the collinear moments.

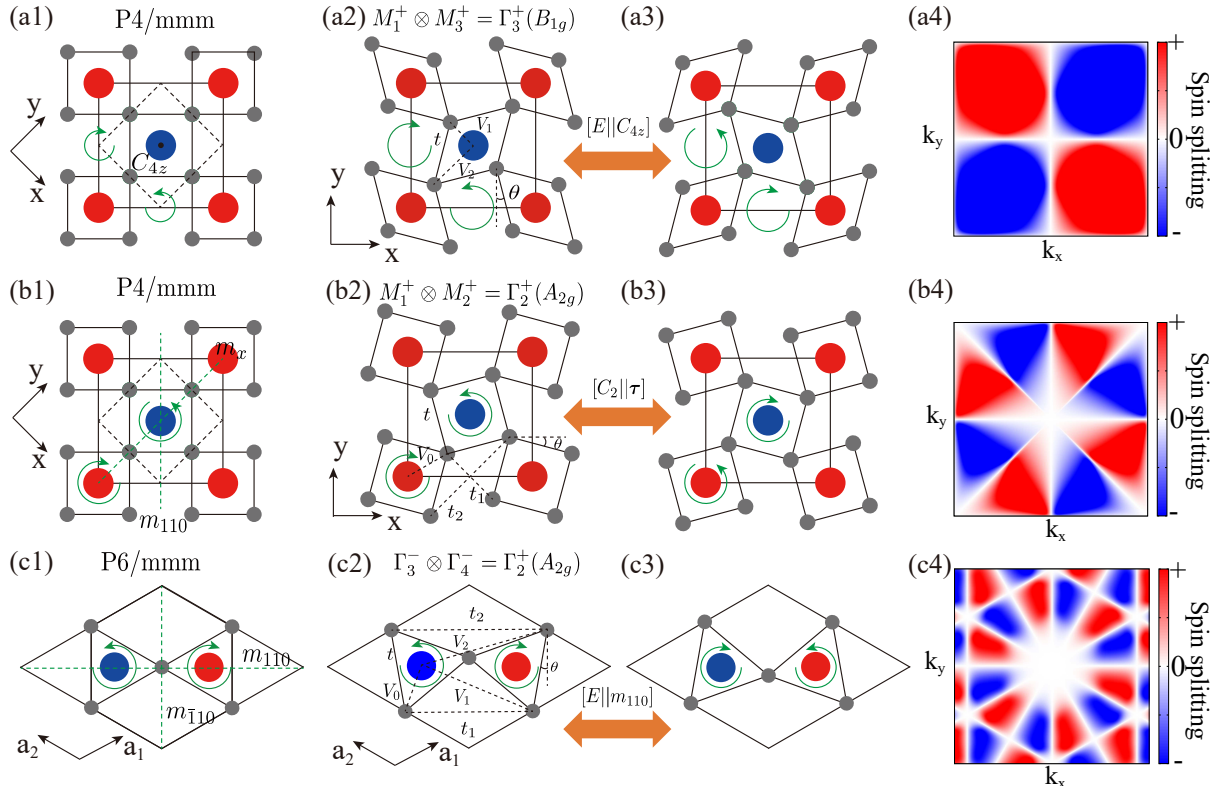


FIG. S1. Ligand-rotation tight-binding models for antiferroaxial altermagnets with d -, planar g -, and planar i -wave altermagnetic spin splitting. Red (blue) spheres denote magnetic sites with spin up (down), gray spheres denote nonmagnetic ligand sites, and green curved arrows indicate the antiferroaxial rotation pattern parametrized by the ligand rotation angle θ . Dashed bonds mark the symmetry-inequivalent hopping/hybridization paths used in Eq. (S-4). (a1)-(a4) d -wave model. (a1) Prototypic parent structure with space group $P4/mmm$. (a2) Structure in the antiferroaxial phase; the coexistence of the Néel order $M_1^+ \otimes M_3^+$ and the antiferroaxial order M_3^+ induces the $\Gamma_3^+(B_{1g})$ multipole channel (corresponding to d_{xy} -type spin splitting). (a3) Configuration with reversed antiferroaxial order ($\theta \rightarrow -\theta$), symmetry-equivalent to applying $[E||C_{4z}]$ to (a2). (a4) Resulting momentum-space spin splitting for (a3), showing the sign reversal relative to (a2), whose spin splitting is plotted in Fig. 2 (a3) in the main text. (b1)-(b4) planar g -wave model. (b1) Parent phase ($P4/mmm$); green dashed lines indicate the mirror planes m_x and m_{110} . (b2) Antiferroaxial structure and the corresponding hopping network; the bilinear $M_1^+ \otimes M_2^+$ yields the $\Gamma_2^+(A_{2g})$ sector, giving a planar g -wave splitting. (b3) Antiferroaxial reversal ($\theta \rightarrow -\theta$), symmetry-equivalent to $[C_2||\tau]$ applied to (b2) with $\tau = (1/2, 1/2, 0)$. (b4) Spin splitting for (b3), with the opposite sign compared to (b2), whose spin splitting is plotted in Fig. 2 (b3) in the main text. (c1)-(c4) planar i -wave model. (c1) Parent structure with $P6/mmm$ symmetry; green dashed lines indicate the mirror planes m_{110} and $m_{1\bar{1}0}$. (c2) Antiferroaxial structure and hopping network; the coexistence of $\mathbf{N} \sim \Gamma_3^- \otimes \Gamma_A^s$ and $\mathbf{G} \sim \Gamma_2^+$ induces the $\Gamma_2^+(A_{2g})$ sector, corresponding to planar i -wave splitting. (c3) Reversed rotation pattern ($\theta \rightarrow -\theta$), symmetry-equivalent to applying $[E||m_{110}]$ to (c2). (c4) Spin splitting for (c3), exhibiting the corresponding sign reversal, whose spin splitting is plotted in Fig. 2 (c3) in the main text. The common model parameters are $J = t$ and $t_M = 0.5t$, with specific values: (a) $\theta = 20^\circ$, $V_1^0 = V_2^0 = 0.6t$. (b) $\theta = 20^\circ$, $V_0 = 1.2t$, $t_1^0 = t_2^0 = 0.25t$. (c) $\theta = 30^\circ$, $V_0 = 1.2t$, $V_1^0 = V_2^0 = 0.5t$, $t_1^0 = t_2^0 = 0.2t$.

A. d -wave antiferroaxial altermagnetic tight-binding model

We construct the d -wave model based on the parent space group $P4/mmm$, as shown in Fig. S1(a1). Both the antiferromagnetic and antiferroaxial instabilities occur at the M point with wavevector $\mathbf{q} = (\pi, \pi, 0)$, transforming as $\mathbf{N} \sim M_1^+$ and $\mathbf{G} \sim M_4^+ \otimes (\Gamma_2^+ \oplus \Gamma_5^+)$, respectively. Here, M_4^+ is the representation of the staggered pattern for the antiferroaxial order, which implies that the clockwise and counterclockwise rotational units are exchanged under C_{4z} and m_x , but remain invariant under m_{110} [the operators are plotted in Fig. S1(b1)]. For the Néel vector, the spin-rotation space representation Γ_A^s is suppressed, as the condition $\Gamma_1^s \subset \Gamma_A^s \otimes \Gamma_A^s$ is always satisfied. The ferroaxial order Γ_A in the point group $4/mmm$ (corresponding to the space group $P4/mmm$) decomposes into the irreducible representation $\Gamma_2^+ \oplus \Gamma_5^+$. For the case with $\mathbf{G} \parallel \hat{z}$, we take $G_z \sim M_4^+ \otimes \Gamma_2^+ = M_3^+$. The bilinear combination then

transforms as

$$\mathbf{N}G_z \sim M_1^+ \otimes M_3^+ = \Gamma_3^+(B_{1g}), \quad (\text{S-5})$$

which enables a symmetry-allowed trilinear invariant with the rank-2 magnetic multipole sector in the parent group. Upon condensation of G_z , the symmetry is reduced to $P4/mbm$ with crystallographic point group $4/mmm$. In this subgroup, the Néel vector, which transforms as M_1^+ in the parent phase, subduces to the one-dimensional irrep B_{2g} . By consulting Table S3, we identify B_{2g} with a d_{xy} -wave altermagnetic spin splitting and the corresponding spin point group $\bar{1}4/m\bar{1}mm$.

In the TB model, we include nearest-neighbor hopping between magnetic atoms (t_M) and between ligand atoms (t). For magnetic-ligand hybridization, we include both nearest- and next-nearest-neighbor hoppings (V_1 and V_2), as illustrated in Fig. S1(a2), which can be modulated by the antiferroaxial distortion angle θ through Harrison's rule [3]

$$\begin{aligned} V_1(\theta) &= V_1^0 \frac{|\mathbf{r}(0)|^2}{|\mathbf{r}(\theta)|^2} = V_1^0 \frac{\sin^2(\pi/4)}{\sin^2(\pi/4 - \theta)} = \frac{V_1^0}{1 - \sin(2\theta)}, \\ V_2(\theta) &= V_2^0 \frac{|\mathbf{r}(0)|^2}{|\mathbf{r}(\theta)|^2} = V_2^0 \frac{\sin^2(\pi/4)}{\sin^2(\pi/4 + \theta)} = \frac{V_2^0}{1 + \sin(2\theta)}, \end{aligned} \quad (\text{S-6})$$

where we assume the ligand-ligand bond length remains constant so that t is independent of θ . The factor $\sin(\pi/4)$ and $\sin(\pi/4 \pm \theta)$ are the hopping distance parameters before and after the distortion, respectively.

Reversing the antiferroaxial order, $\theta \rightarrow -\theta$, yields the structure in Fig. S1(a3). This configuration is symmetry-equivalent to applying $[E||C_{4z}]$ to Fig. S1(a2), where E denotes the identity in spin space and C_{4z} represents a four-fold rotation in real space. As a result, the spin splitting reverses sign, consistent with the reversal of the corresponding magnetic multipole component (cf. Fig. 2(a3) in the main text).

B. g -wave antiferroaxial altermagnetic tight-binding model

For the planar g -wave antiferroaxial altermagnetic model, we consider the tetragonal parent space group $P4/mmm$, as illustrated in Fig. S1(b1), where green dashed lines indicate the m_x and m_{110} mirror planes. In contrast to the d -wave case, the antiferromagnetic and antiferroaxial instabilities here share the same spatial modulation at the M point, i.e., $\Gamma_N(\mathbf{q}') = \Gamma_G(\mathbf{q}) = M_1^+$ with $\mathbf{q} = \mathbf{q}' = (\pi, \pi, 0)$. Consequently, we have $G_z \sim M_1^+ \otimes \Gamma_2^+ = M_2^+$ and $\mathbf{N} \sim M_1^+$. The bilinear combination transforms as

$$\mathbf{N}G_z \sim M_1^+ \otimes M_2^+ = \Gamma_2^+(A_{2g}), \quad (\text{S-7})$$

which allows coupling to the A_{2g} channel of the rank-4 magnetic multipole $\mathbf{O}^{(4)}$ (see Table S1). Upon condensation of G_z , the symmetry is lowered to the isotropy subgroup $P4/mbm$; notably, the crystallographic point group remains $4/mmm$. In this subgroup, the Néel order parameter (originally M_1^+) subduces to the A_{2g} irreducible representation. As listed in Table S3, this representation corresponds to a planar g -wave altermagnetic spin splitting characterized by the spin point group $4/m^1\bar{1}m$.

The Hamiltonian follows Eq. (S-4), with hopping paths shown in Fig. S1(b2). The antiferroaxial rotation angle θ modulates the ligand-ligand hoppings t_1 and t_2 , while the base hoppings' amplitude t and V_0 remain invariant. Their functional forms are given by

$$\begin{aligned} t_1(\theta) &= t_1^0 \frac{\sin^2(\pi/4)}{\sin^2(\pi/4 - \theta)} = \frac{t_1^0}{1 - \sin(2\theta)}, \\ t_2(\theta) &= t_2^0 \frac{\sin^2(\pi/4)}{\sin^2(\pi/4 + \theta)} = \frac{t_2^0}{1 + \sin(2\theta)}, \end{aligned} \quad (\text{S-8})$$

where the factors $\sin(\pi/4)$ and $\sin(\pi/4 \pm \theta)$ in the numerators correspond to the hopping distance parameters before and after the distortion, respectively.

Reversing the antiferroaxial order, $\theta \rightarrow -\theta$, gives the structure in Fig. S1(b3). This configuration is symmetry-equivalent to applying $[C_2||\boldsymbol{\tau}]$ to Fig. S1(b2), where C_2 denotes a π rotation in spin space about an axis perpendicular to the ordered moments and $\boldsymbol{\tau} = (1/2, 1/2, 0)$ is a real-space translation. As a result, the spin splitting reverses sign, as illustrated in Fig. S1(b4) (cf. Fig. 2(b3) in the main text).

C. *i*-wave antiferroaxial altermagnetic tight-binding model

For the planar *i*-wave antiferroaxial altermagnetic model, we adopt the hexagonal parent space group $P6/mmm$, as illustrated in Fig. S1(c1), where the green dashed lines indicate the m_{110} and $m_{\bar{1}10}$ mirror planes. In this hexagonal geometry, both the antiferromagnetic and antiferroaxial instabilities occur at the Γ point. The staggered spatial modulation, which is shared by the Néel and antiferroaxial patterns, transforms as the one-dimensional representation Γ_3^- . Consequently, the Néel vector transforms as $\mathbf{N} \sim \Gamma_3^-$. The antiferroaxial order parameter G_z is constructed by combining this staggered modulation with the axial-vector representation $\Gamma_2^+(A_{2g})$ of the $6/mmm$ point group, yielding $G_z \sim \Gamma_3^- \otimes \Gamma_2^+ = \Gamma_4^-$. The resulting bilinear combination transforms as

$$\mathbf{N}G_z \sim \Gamma_3^- \otimes \Gamma_4^- = \Gamma_2^+(A_{2g}). \quad (\text{S-9})$$

This coupling enables a symmetry-allowed trilinear invariant with the A_{2g} channel of the rank-6 magnetic multipole $\mathbf{O}^{(6)}$ (see Table S1). Upon condensation of G_z , the symmetry is reduced to the isotropy subgroup $P\bar{6}m2$. In this subgroup, the Néel vector (originally Γ_3^-) subduces to the representation A'_2 . As listed in Table S3, this representation corresponds to a planar *i*-wave altermagnetic spin splitting.

The tight-binding Hamiltonian includes the nearest-neighbor hopping between magnetic atoms (t_M), ligand-ligand hopping (t), and magnetic-ligand hybridization (V). The antiferroaxial rotation θ lifts the symmetry of the ligand environment, resulting in two inequivalent ligand-ligand hoppings (t_1, t_2) and two inequivalent magnetic-ligand hybridizations (V_1, V_2), as shown in Fig. S1(c2). Incorporating the structural dependence via Harrison's scaling law, the hopping amplitudes are given by

$$\begin{aligned} t_1(\theta) &= t_1^0 \frac{(\sqrt{3})^2}{2 - 2 \cos(2\pi/3 + 2\theta)} = \frac{3t_1^0}{2[1 + \cos(2\theta - \pi/3)]}, \\ t_2(\theta) &= t_2^0 \frac{(\sqrt{3})^2}{2 - 2 \cos(2\pi/3 - 2\theta)} = \frac{3t_2^0}{2[1 + \cos(2\theta + \pi/3)]}, \\ V_1(\theta) &= V_1^0 \frac{7/3}{4/3 \cos^2 \theta + 1/3 - 4/3 \cos \theta \cos(2\pi/3 + \theta)} = \frac{7V_1^0}{4 + 2\sqrt{3} \sin(2\theta + \pi/3)}, \\ V_2(\theta) &= V_2^0 \frac{7/3}{4/3 \cos^2 \theta + 1/3 - 4/3 \cos \theta \cos(2\pi/3 - \theta)} = \frac{7V_2^0}{4 - 2\sqrt{3} \sin(2\theta - \pi/3)}, \end{aligned} \quad (\text{S-10})$$

where the denominators reflect the changes in bond lengths induced by the distortion angle θ .

Reversing the antiferroaxial order, $\theta \rightarrow -\theta$, yields the structure in Fig. S1(c3). This configuration is related to Fig. S1(c2) by the symmetry operation $[E \parallel m_{\bar{1}10}]$, with E the identity in spin space. Accordingly, the induced $\Gamma_2^+(A_{2g})$ multipole and the associated planar *i*-wave altermagnetic spin splitting change sign under $\theta \rightarrow -\theta$, consistent with the reversal shown in the main text [Fig. 2(c3)].

V. LANDAU THEORY

In this section, we derive an effective Landau functional for cubic perovskites starting from the parent space group $Pm\bar{3}m$, with an emphasis on the R -point structural instability at $\mathbf{q} = (\pi, \pi, \pi)$. This high-symmetry parent phase is shared by a broad class of antiferroaxial altermagnetic materials, including perovskite oxides (e.g., KMnF_3 , LaCrO_3) and transition-metal trifluorides (e.g., FeF_3).

A. Order parameters and symmetry

We introduce the following order parameters, classified by the irreducible representations (IRs) of the parent space group at the R point:

- Néel order.** The antiferromagnetic order parameter is denoted by the spin-space vector \mathbf{N} and transforms as $\mathbf{N} \sim R_1^+$. Throughout this section, we take the zero SOC limit, the direction of \mathbf{N} is decoupled from the real space, and we treat its amplitude $N \equiv |\mathbf{N}|$ as the relevant Landau variable.
- Antiferroaxial order.** The antiferroaxial (counter-rotating) distortion is described by a three-component axial order parameter $\mathbf{G} = (G_x, G_y, G_z)$ transforming as $\mathbf{G} \sim R_1^+ \otimes \Gamma_4^+(T_{1g}) = R_4^+$.

3. Elastic strains. Since \mathbf{G} is a structural order parameter, the lattice strains ε_{ij} constitute additional symmetry-allowed secondary degrees of freedom and generally couple to \mathbf{G} via rotostriction, thereby renormalizing the effective Landau coefficients and generating anisotropy. We therefore include the symmetric strain tensor ε_{ij} and decompose it into symmetry-adapted combinations of the cubic point group O_h :

$$A_{1g} : \quad \varepsilon_v = \varepsilon_{xx} + \varepsilon_{yy} + \varepsilon_{zz}, \quad (\text{S-11})$$

$$E_g : \quad \varepsilon_1 = \varepsilon_{zz} - \frac{1}{2}(\varepsilon_{xx} + \varepsilon_{yy}), \quad \varepsilon_2 = \frac{\sqrt{3}}{2}(\varepsilon_{yy} - \varepsilon_{xx}), \quad (\text{S-12})$$

$$T_{2g} : \quad (\varepsilon_{yz}, \varepsilon_{xz}, \varepsilon_{xy}). \quad (\text{S-13})$$

4. Rank-4 (g-wave) magnetic multipoles. The antiferroaxial altermagnetic order is diagnosed by the rank $\ell = 4$ magnetic multipole in the T_{1g} spatial channel. We choose a convenient basis

$$(\mathbf{O}_1, \mathbf{O}_2, \mathbf{O}_3) = (\mathbf{O}_{yz(y^2-z^2)}, \mathbf{O}_{xz(x^2-z^2)}, \mathbf{O}_{xy(x^2-y^2)}), \quad (\text{S-14})$$

where each \mathbf{O}_i is a spin-space vector defined microscopically by $\mathbf{O}_{xy(x^2-y^2)} \equiv \int d^3r xy(x^2 - y^2) \mathbf{m}(\mathbf{r})$, and similarly for the other components.

Because \mathbf{N} and \mathbf{O}_i are both vectors in spin space, all dot products below are taken in spin space.

B. Landau free energy

The total free-energy density, which can be constructed using the symmetry analysis tools in the ISOTROPY software suite [4, 5], is given by

$$\mathcal{F} = \mathcal{F}_{N,G} + \mathcal{F}_\varepsilon + \mathcal{F}_{G\varepsilon} + \mathcal{F}_{N,G,O}. \quad (\text{S-15})$$

We first collect the magnetic and antiferroaxial contributions. Keeping terms up to quartic order, we write

$$\mathcal{F}_{N,G} = \alpha_N \mathbf{N}^2 + \beta_N (\mathbf{N}^2)^2 + \alpha_G \mathbf{G}^2 + \beta_{G1} (\mathbf{G}^2)^2 + \beta_{G2} (G_x^2 G_y^2 + G_x^2 G_z^2 + G_y^2 G_z^2) + \lambda_{NG} \mathbf{N}^2 \mathbf{G}^2, \quad (\text{S-16})$$

where $\mathbf{G}^2 = G_x^2 + G_y^2 + G_z^2$.

The elastic energy at the harmonic level allowed by O_h is

$$\mathcal{F}_\varepsilon = C_0 \varepsilon_v^2 + C_1 (\varepsilon_1^2 + \varepsilon_2^2) + C_2 (\varepsilon_{yz}^2 + \varepsilon_{xz}^2 + \varepsilon_{xy}^2). \quad (\text{S-17})$$

The bilinear coupling between the quadratic form of \mathbf{G} and the strain irreducible representations is

$$\mathcal{F}_{G\varepsilon} = \lambda_1 \left[\frac{1}{\sqrt{3}} (2G_z^2 - G_x^2 - G_y^2) \varepsilon_1 + (G_x^2 - G_y^2) \varepsilon_2 \right] + \lambda_2 (G_y G_z \varepsilon_{yz} + G_x G_z \varepsilon_{xz} + G_x G_y \varepsilon_{xy}). \quad (\text{S-18})$$

An additional A_{1g} coupling $\propto \mathbf{G}^2 \varepsilon_v$ is symmetry-allowed and can be absorbed into a redefinition of β_{G1} .

Finally, the lowest-order invariant coupling among \mathbf{N} , \mathbf{G} , and the T_{1g} multipoles reads

$$\mathcal{F}_{N,G,O} = \lambda_O (\mathbf{O}_1^2 + \mathbf{O}_2^2 + \mathbf{O}_3^2) + g \mathbf{N} \cdot (G_x \mathbf{O}_1 + G_y \mathbf{O}_2 + G_z \mathbf{O}_3). \quad (\text{S-19})$$

Once both $\mathbf{N} \neq 0$ and $\mathbf{G} \neq 0$ develop, this term induces the g -wave multipole as $\mathbf{O}_i \propto \mathbf{N} G_i$, implying an antiferroaxial control of the altermagnetic spin splitting.

C. Integrating out secondary degrees of freedom

We now derive an effective free energy in terms of the primary structural order parameter \mathbf{G} by eliminating \mathbf{O} , \mathbf{N} (amplitude), and the strains ε through their saddle-point conditions.

1. Eliminating the multipoles \mathbf{O}

Minimizing Eq. (S-19) with respect to \mathbf{O}_i gives

$$\frac{\partial \mathcal{F}}{\partial \mathbf{O}_i} = 0 \quad \Rightarrow \quad \mathbf{O}_i = -\frac{g}{2\lambda_O} \mathbf{N} G_i. \quad (\text{S-20})$$

Substituting back into Eq. (S-19) yields a negative biquadratic contribution

$$\mathcal{F}_{N,G,O} \rightarrow -\frac{g^2}{4\lambda_O} \mathbf{N}^2 \mathbf{G}^2. \quad (\text{S-21})$$

Therefore the effective $\mathbf{N}^2 \mathbf{G}^2$ coupling becomes

$$\Lambda \equiv \lambda_{NG} - \frac{g^2}{4\lambda_O}. \quad (\text{S-22})$$

2. Eliminating the Néel amplitude N

After eliminating \mathbf{O} , the N -dependent part is

$$\mathcal{F}_N = \alpha_N \mathbf{N}^2 + \beta_N (\mathbf{N}^2)^2 + \Lambda \mathbf{N}^2 \mathbf{G}^2. \quad (\text{S-23})$$

Stationarity $\partial \mathcal{F}/\partial \mathbf{N} = 0$ gives

$$\alpha_N \mathbf{N} + 2\beta_N \mathbf{N}^2 \mathbf{N} + \Lambda \mathbf{G}^2 \mathbf{N} = 0. \quad (\text{S-24})$$

In the magnetically ordered phase ($\mathbf{N} \neq 0$) this yields

$$\mathbf{N}^2 = -\frac{\alpha_N + \Lambda \mathbf{G}^2}{2\beta_N}. \quad (\text{S-25})$$

Substituting Eq. (S-25) back contributes the standard negative-definite term

$$\mathcal{F}_N \rightarrow -\frac{(\alpha_N + \Lambda \mathbf{G}^2)^2}{4\beta_N} = \text{const.} - \frac{\alpha_N \Lambda}{2\beta_N} \mathbf{G}^2 - \frac{\Lambda^2}{4\beta_N} (\mathbf{G}^2)^2. \quad (\text{S-26})$$

3. Eliminating strains

Minimizing $\mathcal{F}_\varepsilon + \mathcal{F}_{G\varepsilon}$ with respect to each strain component gives

$$\begin{aligned} \varepsilon_1 &= -\frac{\lambda_1}{2C_1} \frac{1}{\sqrt{3}} (2G_z^2 - G_x^2 - G_y^2), & \varepsilon_2 &= -\frac{\lambda_1}{2C_1} (G_x^2 - G_y^2), \\ \varepsilon_{ij} &= -\frac{\lambda_2}{2C_2} G_i G_j, & (i \neq j; i, j \in \{x, y, z\}), \end{aligned} \quad (\text{S-27})$$

while ε_v decouples in the present truncation. Substituting (S-27) back yields the strain-mediated quartic renormalization

$$\Delta \mathcal{F}_{\text{strain}} = -\frac{\lambda_1^2}{3C_1} (\mathbf{G}^2)^2 + \left(\frac{\lambda_1^2}{C_1} - \frac{\lambda_2^2}{4C_2} \right) (G_x^2 G_y^2 + G_x^2 G_z^2 + G_y^2 G_z^2). \quad (\text{S-28})$$

D. Effective free energy for \mathbf{G}

Collecting the above results, the effective free energy takes the cubic-invariant form

$$\mathcal{F}_{\text{eff}}(\mathbf{G}) = \alpha_{\text{eff}} \mathbf{G}^2 + \beta_{1,\text{eff}} (\mathbf{G}^2)^2 + \beta_{2,\text{eff}} (G_x^2 G_y^2 + G_x^2 G_z^2 + G_y^2 G_z^2), \quad (\text{S-29})$$

with renormalized coefficients

$$\alpha_{\text{eff}} = \alpha_G - \frac{\alpha_N}{2\beta_N} \Lambda, \quad (\text{S-30})$$

$$\beta_{1,\text{eff}} = \beta_{G1} - \frac{\Lambda^2}{4\beta_N} - \frac{\lambda_1^2}{3C_1}, \quad (\text{S-31})$$

$$\beta_{2,\text{eff}} = \beta_{G2} + \frac{\lambda_1^2}{C_1} - \frac{\lambda_2^2}{4C_2}. \quad (\text{S-32})$$

The anisotropy parameter $\beta_{2,\text{eff}}$ determines the orientation of \mathbf{G} and therefore the form of the induced g -wave multipole.

E. Phase I: $\mathbf{G} \parallel [001]$ (planar g -wave)

For $\beta_{2,\text{eff}} > 0$, the minimum is achieved when \mathbf{G} points along a principal axis, e.g. $\mathbf{G} = (0, 0, G_z)$. Then Eq. (S-29) reduces to

$$\mathcal{F}_{\text{eff}} = \alpha_{\text{eff}} G_z^2 + \beta_{1,\text{eff}} G_z^4, \quad (\text{S-33})$$

with $G_z^2 = -\alpha_{\text{eff}}/(2\beta_{1,\text{eff}})$ in the ordered phase. Stability against transverse fluctuations requires $\beta_{1,\text{eff}} > 0$ and $\beta_{2,\text{eff}} > 0$.

The secondary orders follow from Eq. (S-20), Eq. (S-25), and Eq. (S-27):

$$\mathbf{O}_3 = -\frac{g}{2\lambda_O} \mathbf{N} G_z \neq 0, \quad \mathbf{O}_1 = \mathbf{O}_2 = 0, \quad \mathbf{N}^2 = -\frac{\alpha_N + \Lambda G_z^2}{2\beta_N}, \quad (\text{S-34})$$

indicating a planar g -wave multipole with $xy(x^2 - y^2)$ spin-splitting form. The equilibrium strains are

$$\varepsilon_2 = \varepsilon_{xy} = \varepsilon_{xz} = \varepsilon_{yz} = 0, \quad \varepsilon_1 = -\frac{\lambda_1}{C_1 \sqrt{3}} G_z^2. \quad (\text{S-35})$$

When coupling to uniaxial stress along [001]. Applying a uniaxial stress σ_z adds $\mathcal{F}_{\text{stress}} = -\sigma_z \varepsilon_{zz}$. Using $\varepsilon_{zz} = \varepsilon_v/3 + 2\varepsilon_1/3$, only ε_1 is relevant here. The minimization condition becomes

$$2C_1 \varepsilon_1 + \frac{\lambda_1}{\sqrt{3}} (2G_z^2) - \frac{2}{3} \sigma_z = 0 \quad \Rightarrow \quad \varepsilon_1 = -\frac{\lambda_1}{C_1 \sqrt{3}} G_z^2 + \frac{\sigma_z}{3C_1}. \quad (\text{S-36})$$

Substituting this solution back, the stress generates a linear shift of the quadratic coefficient,

$$\alpha_{\text{eff}}(\sigma_z) = \alpha_{\text{eff}}(0) + \frac{2\lambda_1}{3\sqrt{3}C_1} \sigma_z. \quad (\text{S-37})$$

This leads to the relation $G_z \propto \sqrt{\sigma_z - \sigma_c}$, valid for $\lambda_1 \sigma_z > 0$, where the critical threshold is given by $\sigma_c = -\frac{3\sqrt{3}C_1}{2\lambda_1} \alpha_{\text{eff}}(0)$. This result demonstrates that the antiferroaxial order—and consequently the altermagnetism—can be mechanically controlled on or off. This scenario is realized in KMnF₃ [Fig. S5(d)].

F. Phase II: $\mathbf{G} \parallel [111]$ (bulk g -wave)

For $\beta_{2,\text{eff}} < 0$, the minimum is achieved for the body-diagonal configuration $G_x = G_y = G_z = G/\sqrt{3}$, yielding

$$\mathcal{F}_{\text{eff}} = \alpha_{\text{eff}} G^2 + \beta_{\text{eff}} G^4, \quad \beta_{\text{eff}} \equiv \beta_{1,\text{eff}} + \frac{1}{3} \beta_{2,\text{eff}}, \quad (\text{S-38})$$

and $G^2 = -\alpha_{\text{eff}}/(2\beta_{\text{eff}})$. The induced multipoles are equal-amplitude

$$\mathbf{O}_1 = \mathbf{O}_2 = \mathbf{O}_3 = -\frac{g}{2\lambda_O} \mathbf{N} \frac{G}{\sqrt{3}}, \quad (\text{S-39})$$

corresponding to the coherent superposition $yz(y^2 - z^2) + zx(z^2 - x^2) + xy(x^2 - y^2) = (x + y + z)(x - y)(y - z)(z - x)$, i.e., the bulk g -wave form.

In this phase the E_g -type strains vanish, hence $\varepsilon_1 = \varepsilon_2 = 0$, while the T_{2g} shear strains satisfy

$$\varepsilon_{xy} = \varepsilon_{yz} = \varepsilon_{xz} \equiv \varepsilon_s = -\frac{\lambda_2}{6C_2} G^2. \quad (\text{S-40})$$

Stress along [111] and anharmonic elasticity. Under uniaxial stress σ_{111} , the relevant combination is $\varepsilon_{111} = \frac{1}{3}\varepsilon_v + 2\varepsilon_s$, giving $\mathcal{F}_{\text{stress}} = -(\sigma_{111}/3)\varepsilon_v - 2\sigma_{111}\varepsilon_s$. Because $\varepsilon_s \neq 0$, the lowest shear-anharmonic invariant $C_3\varepsilon_{xy}\varepsilon_{yz}\varepsilon_{xz} = C_3\varepsilon_s^3$ contributes. The shear-sector free energy becomes

$$\mathcal{F}_s = 3C_2\varepsilon_s^2 + C_3\varepsilon_s^3 + \lambda_2 G^2 \varepsilon_s - 2\sigma_{111}\varepsilon_s. \quad (\text{S-41})$$

Minimizing with respect to ε_s gives

$$(\lambda_2 G^2 - 2\sigma_{111}) + 6C_2\varepsilon_s + 3C_3\varepsilon_s^2 = 0. \quad (\text{S-42})$$

For weak anharmonicity $|C_3| \ll C_2$, the solution satisfying $\varepsilon_s \rightarrow 0$ when $G, \sigma_{111} \rightarrow 0$ reads

$$\varepsilon_s(\sigma_{111}) \simeq \frac{2\sigma_{111} - \lambda_2 G^2}{6C_2} - \frac{C_3}{72C_2^3} (2\sigma_{111} - \lambda_2 G^2)^2. \quad (\text{S-43})$$

Substituting back, the stress effectively renormalizes the quadratic and quartic coefficients (up to $O(G^4)$ and keeping the leading stress dependence):

$$\alpha_{\text{eff}}(\sigma_{111}) = \alpha_{\text{eff}}(0) + \frac{\lambda_2}{3C_2} \sigma_{111} - \frac{C_3 \lambda_2}{18C_2^3} \sigma_{111}^2, \quad (\text{S-44})$$

$$\beta_{\text{eff}}(\sigma_{111}) = \beta_{\text{eff}}(0) + \frac{C_3 \lambda_2^2}{36C_2^3} \sigma_{111}, \quad (\text{S-45})$$

which implies a generically non-monotonic (parabolic) dependence of G^2 on σ_{111} (or strain, as stress and strain satisfy Hooke's law in the small-strain limit). This provides an analytic rationale for the parabolic strain dependence of the antiferroaxial rotation amplitude observed in FeF_3 , as shown in Fig. S2.

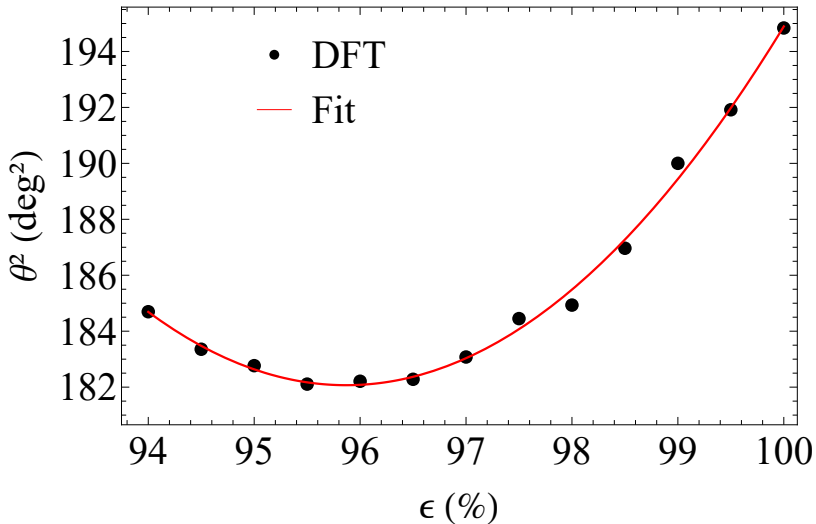


FIG. S2. Dependence of the squared antiferroaxial rotation angle θ^2 on the applied uniaxial strain ε_{111} in FeF_3 , obtained from DFT calculations. The numerical results are well fit to the quadratic relation $\theta^2 = 7085 - 144\varepsilon_{111} + 0.7511\varepsilon_{111}^2$, where θ is expressed in degrees and the strain ε_{111} is expressed in percentage.

VI. COMPUTATIONAL DETAILS AND CANDIDATE ANTIFERROAXIAL ALTERMAGNETS

A. First-principles calculations and Wannier-based tight-binding models

The first-principles calculations of structure optimization and band structures are using Vienna *ab initio* simulation package(VASP)[6]. The generalized gradient approximation (GGA) with Perdew-Burke-Ernzerhof (PBE)[7] realization is considered. For correlated 3d orbitals, a Hubbard U correction was employed as specified for each material below.

To evaluate Berry-curvature-related responses (e.g., anomalous Hall conductivity in FeF_3), we constructed *ab initio* tight-binding Hamiltonians based on maximally localized Wannier functions using Wannier90 code [8]. Unless otherwise stated, the nonrelativistic altermagnetic spin splitting discussed in this work is analyzed in the zero SOC limit. In this section, we suppress the axial-vector representation Γ_A^s in spin-rotational space.

In this section, we provide the computational details, symmetry analyses, and calculated physical properties for all candidate antiferroaxial altermagnets identified in this work, including MnS_2 , MnC_2 , FeBr_3 , KMnF_3 , Ca_2MnO_4 , FeF_3 , CoF_3 , LaCrO_3 , and La_2NiO_4 .

B. 2D pentagonal planar g -wave altermagnets: MnA_2 ($\mathbf{A} = \mathbf{S}, \mathbf{C}$)

Figure S3 summarizes the crystal structures, magnetic configurations, and electronic band structures of the 2D pentagonal systems MnS_2 and MnC_2 [9]. The parent phase belongs to the space group $P\bar{4}m2$, where the primitive cell contains a magnetic Mn atom coordinated by nonmagnetic ligands, forming a M-A₄ ($\mathbf{A}=\mathbf{S}, \mathbf{C}$) tetrahedral unit with S_{4z} symmetry. Both the antiferromagnetic and antiferroaxial instabilities occur at the M point $\mathbf{q} = (\pi, \pi, 0)$, yielding a C-type antiferromagnetic order. In the zero SOC limit, the Néel vector transforms as $\mathbf{N} \sim M_1$, and the antiferroaxial order corresponds to the counter-rotation of neighboring ligand tetrahedra around the z axis, characterized by a staggered axial vector G_z transforming as $G_z \sim M_2$. Consequently, their bilinear product transforms as a Γ -point representation,

$$G_z \mathbf{N} \sim M_1 \otimes M_2 = \Gamma_2(A_2), \quad (\text{S-46})$$

and thus couples to the A_2 component of the rank four multipoles,

$$\mathbf{O}^{(4)} \sim 2A_1 \oplus A_2 \oplus B_1 \oplus B_2 \oplus 2E. \quad (\text{S-47})$$

The isotropy subgroup is $P\bar{4}2_1m$, in which the subduced Néel order transforms as $\Gamma_2(A_2)$, resulting in the planar g -wave altermagnetic spin splitting according to Table S3, consistent with DFT results shown in Fig. S3(c,f).

Computational details: For MnS_2 and MnC_2 , we used $U = 4$ eV on Mn 3d orbitals. The Brillouin zone was sampled using a $13 \times 13 \times 1$ k mesh, and the plane-wave cutoff energy was set to 550 eV.

C. 2D planar i -wave altermagnet: 2H- FeBr_3

Figure S4 shows the structure and band structure of 2H- FeBr_3 [10]. The parent phase belongs to $P6/mmm$, where in the parent phase Fe atoms form a honeycomb lattice and Br atoms form a Kagome network [Fig. S4(a)]. The two Fe sublattices (spin up/down) are related by spatial inversion in the parent phase, and the collinear Néel vector transforms as Γ_3^- in the zero SOC limit. The antiferroaxial transition corresponds to the counter-rotation of Br ligands around the two inversion-related Fe sites, which transforms as $G_z \sim \Gamma_3^- \otimes \Gamma_2^+ = \Gamma_4^-$. Consequently, their bilinear product transforms as

$$G_z \mathbf{N} \sim \Gamma_3^- \otimes \Gamma_4^- = \Gamma_2^+(A_{2g}), \quad (\text{S-48})$$

and thus couples to the A_{2g} component of the rank six multipoles,

$$\mathbf{O}^{(6)} \sim A_{1g} \oplus A_{2g} \oplus E_g \oplus T_{1g} \oplus 2T_{2g}. \quad (\text{S-49})$$

The isotropy subgroup is $P\bar{6}m2$, in which the subduced Néel order transforms as $\Gamma_2(A'_2)$, resulting in the planar i -wave altermagnetic spin splitting according to Table S3, consistent with DFT results shown in Fig. S4(c)

Computational details: We used $U = 5$ eV on Fe 3d orbitals, a $13 \times 13 \times 1$ k mesh, and a plane-wave cutoff energy of 550 eV.

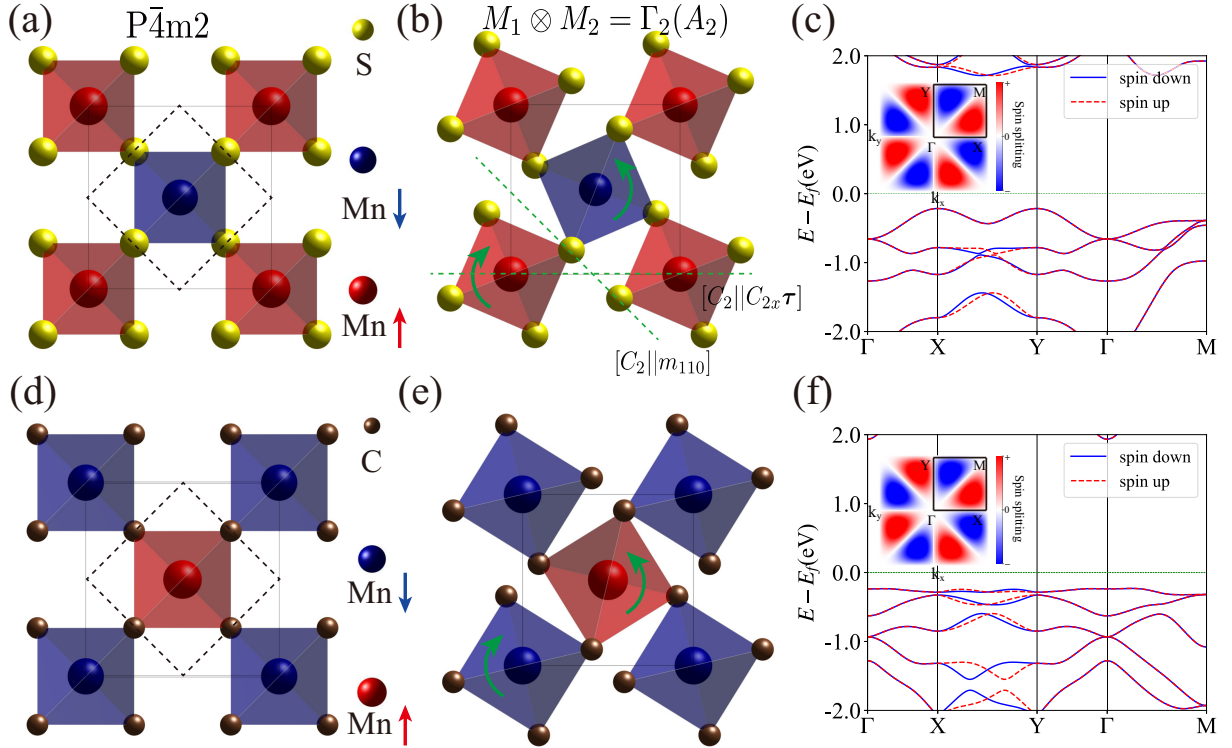


FIG. S3. Structural transition and electronic structure of MnA_2 ($\text{A}=\text{S}, \text{C}$). (a,d) Parent phase (space group $P\bar{4}m2$). The primitive cell is shown in dashed lines. Red/blue Mn spheres denote opposite spins; yellow/brown spheres denote nonmagnetic ligands forming a tetrahedra. The Néel vector transforms as M_1 . (b,e) Antiferroaxial phase with counter-rotating ligand tetrahedra, described by $G_z \sim M_2$. After G_z condensed, two opposite magnetic Mn atoms can be connected through spin group operator $[C_2|m_{110}]$ and $[C_2||C_{2x}\tau]$, where $\tau = (1/2, 1/2, 0)$. (c,f) Band structures exhibiting planar g -wave altermagnetic spin splitting in the antiferroaxial phase (isotropy subgroup $P\bar{4}2_1m$), where the Néel order subduces to $\Gamma_2(A_2)$.

D. 3D planar g -wave altermagnets: KMnF_3 and Ca_2MnO_4

KMnF_3 [11] is a representative perovskite-based planar g -wave altermagnet. The antiferroaxial order is realized by a staggered rotation of corner-sharing MnF_6 octahedra, which we parameterize by the rotation angle θ , and the magnetic ground state is the G -type antiferromagnet [Fig. S5(a)]. Within the Landau description in Sec. V, the planar character is selected when the antiferroaxial anisotropy favors a principal-axis configuration, e.g., $\mathbf{G} \parallel \hat{z}$, which yields the planar g -wave spin-splitting form.

Starting from the cubic parent space group $Pm\bar{3}m$, both the antiferroaxial distortion and the Néel order are associated with the R point. Their condensation lowers the symmetry to the isotropy subgroup $I4/mcm$, leading to a planar g -wave altermagnetic spin splitting in the $xy(x^2 - y^2)$ channel. The energetic barrier of the antiferroaxial distortion is quantified by the DFT total-energy profile as a function of θ [Fig. S5(c)]. By fitting this $E(\theta)$ curve, we extract an effective Landau free energy for the antiferroaxial order. Finally, we demonstrate that epitaxial strain provides an efficient tuning knob for the antiferroaxial order: the distortion can be switched on or suppressed by strain, and the magnitude obeys an approximately linear relation $\mathbf{G}^2 \propto \theta^2 \sim \varepsilon$ [Fig. S5(d)], consistent with the strain-coupling analysis in Sec. V. When $\varepsilon_{zz} < 94.5\%$, the angle $\theta = 0$. Consequently, the spin splitting vanishes, and the system effectively reduces to a $T\tau$ -invariant antiferromagnet.

Computational details (KMnF_3): We used $U = 5$ eV on Mn, a $7 \times 7 \times 5$ k mesh, and a plane-wave cutoff energy of 550 eV.

Ca_2MnO_4 crystallizes in the Ruddlesden-Popper perovskite structure [12], and exhibits an analogous planar antiferroaxial rotation of MnO_6 octahedra around \hat{z} . This distortion lowers the symmetry from the parent space group $I4/mmm$ to isotropy subgroup $I4_1/acd$ and induces planar g -wave altermagnetic spin splitting. It exhibits an analogous planar antiferroaxial rotation of Mn-O_6 octahedra around z , as shown in Figs. S6(a) and (b). Both antiferroaxial and antiferromagnetic phase transitions occur at the P point with propagation vector $\mathbf{q} = (1/4, 1/4, 1/4)$, corresponding to the irreducible representations $G_z \sim P_2$ and $\mathbf{N} \sim P_1$, respectively. Upon condensation of G_z , the symmetry is lowered to the space group $I4_1/acd$. In this phase, the Néel vector transforms as $\mathbf{N} \sim \Gamma_2^+(A_{2g})$, which corresponds to

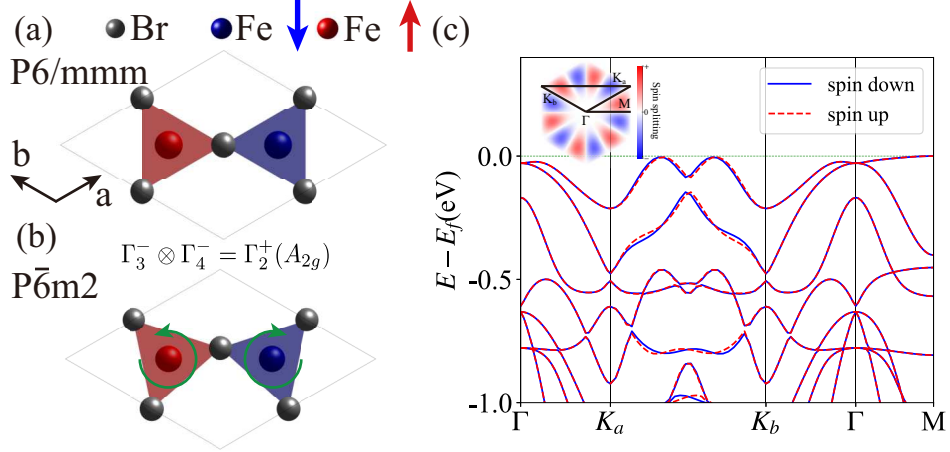


FIG. S4. Antiferroaxial transition and planar *i*-wave altermagnetism in 2H-FeBr₃. (a) Parent phase (space group *P*6/*mmm*) with Fe honeycomb and Br Kagome sublattices. The Néel vector transforms as Γ_3^- . (b) Antiferroaxial phase: counter-rotation of Br ligands described by $G_z \sim \Gamma_4^-$, lowering the symmetry to *P*6m2. (c) Band structure exhibiting the planar *i*-wave altermagnetic spin splitting in the antiferroaxial phase.

a planar *g*-wave altermagnetism characterized by the $xy(x^2 - y^2)$ symmetry [Table S3], as illustrated in Fig. S6(c). *Computational details (Ca₂MnO₄):* We used $U = 3$ eV on Mn and a $9 \times 9 \times 3$ k mesh (cutoff 550 eV).

E. 3D bulk *g*-wave altermagnets: MF₃ (M = Fe, Co, Ni) and LaCrO₃

FeF₃ [Fig. S7] and its isostructural counterparts (CoF₃, NiF₃) host a bulk antiferroaxial distortion of corner-sharing M-F₆ octahedra [13, 14]. The high-temperature parent phase is *Pm*3*m*. At low temperatures, both antiferroaxial and antiferromagnetic instabilities occur at the *R* point $\mathbf{q} = (\pi, \pi, \pi)$. Symmetry analysis gives $\mathbf{G} \sim R_4^+$, $\mathbf{N} \sim R_1^+$, so that the bilinear combination transforms as $\mathbf{GN} \sim R_4^+ \otimes R_1^+ = \Gamma_4^+(T_{1g})$. Since the rank four magnetic multipole contains the T_{1g} spatial channel, a symmetry-allowed trilinear coupling is present, stabilizing a bulk *g*-wave altermagnetic state.

The antiferroaxial magnitude is parameterized by the octahedral rotation angle θ . The total-energy profile exhibits a double-well potential with degenerate minima at $\theta = \pm 12^\circ$ and a barrier of order $\Delta E \sim 30$ meV. The two antiferroaxial domains are related by a spin-group operation $[C_2||\tau]$ with $\tau = (0, 0, 1/2)$, enforcing a sign reversal of the nonrelativistic spin splitting upon $\theta \rightarrow -\theta$. With SOC included, the two domains are related by $\mathcal{T}\tau$, implying that all time-reversal-odd response functions (e.g., anomalous Hall conductivity) must also reverse sign, as shown in Fig. S7(d).

For FeF₃, the anomalous Hall conductivity was evaluated using a Wannier-interpolated tight-binding model and the standard Kubo formula [15, 16],

$$\sigma_{xy} = \frac{e^2}{\hbar} \int_{BZ} \frac{d^3k}{(2\pi)^3} \sum_{m \neq n} (f_{m\mathbf{k}} - f_{n\mathbf{k}}) \frac{\text{Im}[\langle \psi_{n\mathbf{k}} | v_x | \psi_{m\mathbf{k}} \rangle \langle \psi_{m\mathbf{k}} | v_y | \psi_{n\mathbf{k}} \rangle]}{(E_{m\mathbf{k}} - E_{n\mathbf{k}})^2}, \quad (\text{S-50})$$

where $v_\alpha = \partial H_{\mathbf{k}} / \partial k_\alpha$ ($\alpha = x, y$), $f_{n\mathbf{k}}$ is the Fermi-Dirac distribution, and $E_{n\mathbf{k}}$ denotes the band energy.

Computational details (FeF₃): We used $U = 5$ eV on Fe 3d orbitals and a plane-wave cutoff energy of 550 eV. The Brillouin-zone sampling was chosen consistently for a 3D bulk primitive cell.

LaCrO₃ [Fig. S8] [17] and CoF₃ [Fig. S9] shares the same R_4^+ -type octahedral rotation mode and therefore realizes the same bulk *g*-wave antiferroaxial altermagnetism [Fig. S8 and Fig. S9]. For LaCrO₃ and CoF₃, we used $U = 3$ eV for Cr in LaCrO₃ and $U = 6$ eV for Co in CoF₃, respectively (cutoff 550 eV).

F. 3D *d*-wave altermagnet: La₂NiO₄

La₂NiO₄ is a Ruddlesden-Popper compound with parent space group *I*4/*mmm* [18]. Symmetry-mode analysis indicates concomitant antiferroaxial and antiferromagnetic instabilities at the *X* point $\mathbf{q} = (\pi, \pi, 0)$, yielding $G_{110} \sim$

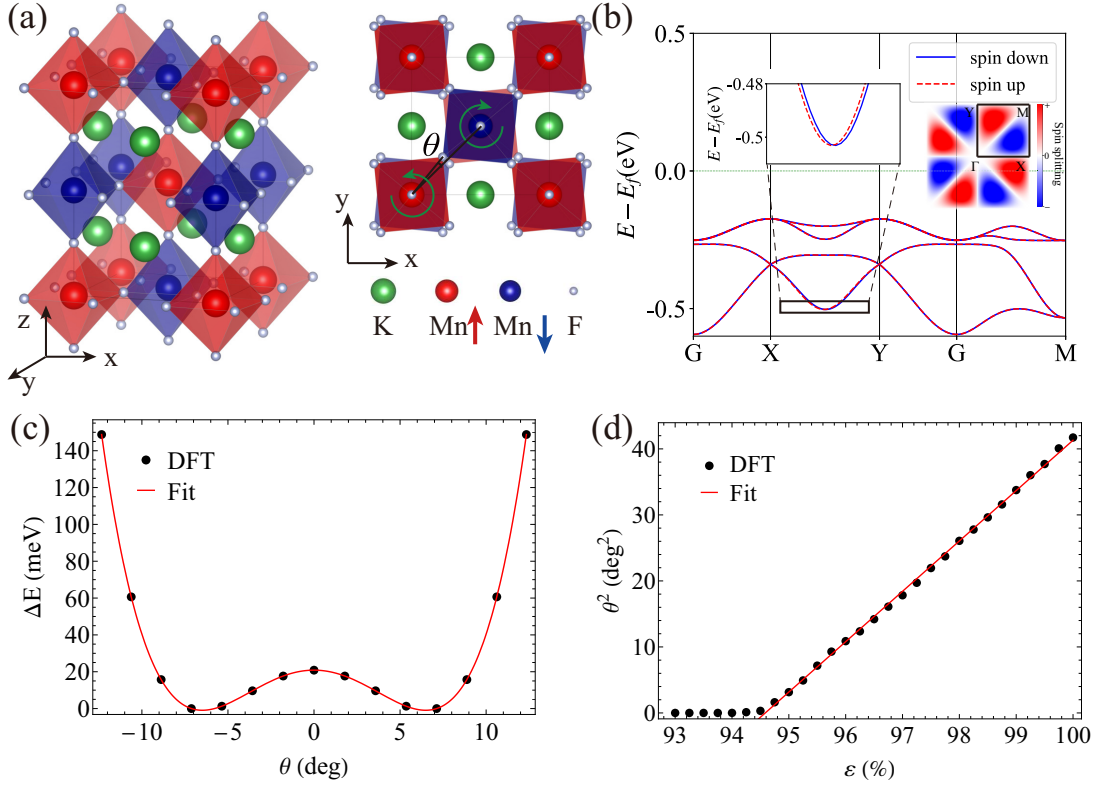


FIG. S5. Structure, electronic properties, and energetics of the planar *g*-wave altermagnet KMnF₃. (a) Crystal structure illustrating the staggered rotation of corner-sharing MnF₆ octahedra about the *z* axis; red and blue octahedra denote the spin-up and spin-down sublattices, respectively. (b) Electronic band structure exhibiting the characteristic planar *g*-wave altermagnetic spin splitting; the bands remain doubly degenerate along Γ -X, Γ -Y, and Γ -M. (c) DFT total energy as a function of the octahedral rotation angle θ (black dots), fitted by an effective Landau potential (red line). The fitted free energy per unit cell is $\mathcal{F}_{\text{eff}}(\theta) = 20.8575 - 1.03319\theta^2 + 0.0122299\theta^4$, where \mathcal{F}_{eff} is in meV per unit cell and θ is in degrees. (d) Strain dependence of the structural order parameter: θ^2 as a function of the uniaxial strain ε_{zz} . Black dots are DFT data and the red line is a linear fit, $\theta^2 = -721.634 + 7.62945\varepsilon_{zz}$ (with θ in degrees and ε_{zz} in percent). When $\varepsilon_{zz} < 94.5\%$, the angle $\theta = 0$. Consequently, the spin splitting vanishes, and the system effectively reduces to a $T\tau$ -invariant antiferromagnet.

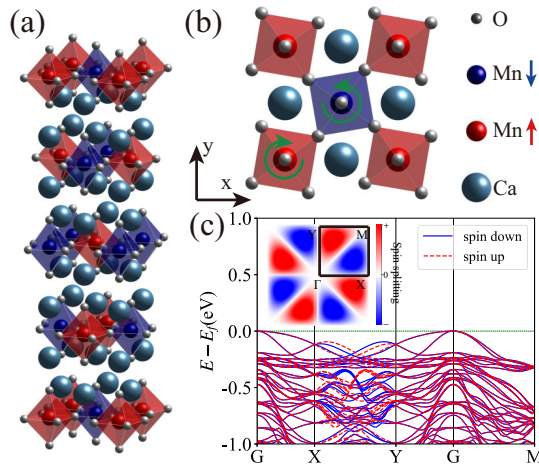


FIG. S6. The structure, antiferroaxial distortion and band structure of Ca₂MnO₄. (a) Crystal structure of Ca₂MnO₄ (parent space group *I*4/*mmm*) with spin-up (red) and spin-down (blue) sublattices. (b) The antiferroaxial distortion $G_z \sim P_2$ characterized by the counter-rotation of Mn-O₆ octahedra around the *z*-axis. (c) Band structure exhibiting planar *g*-wave altermagnetic spin splitting.

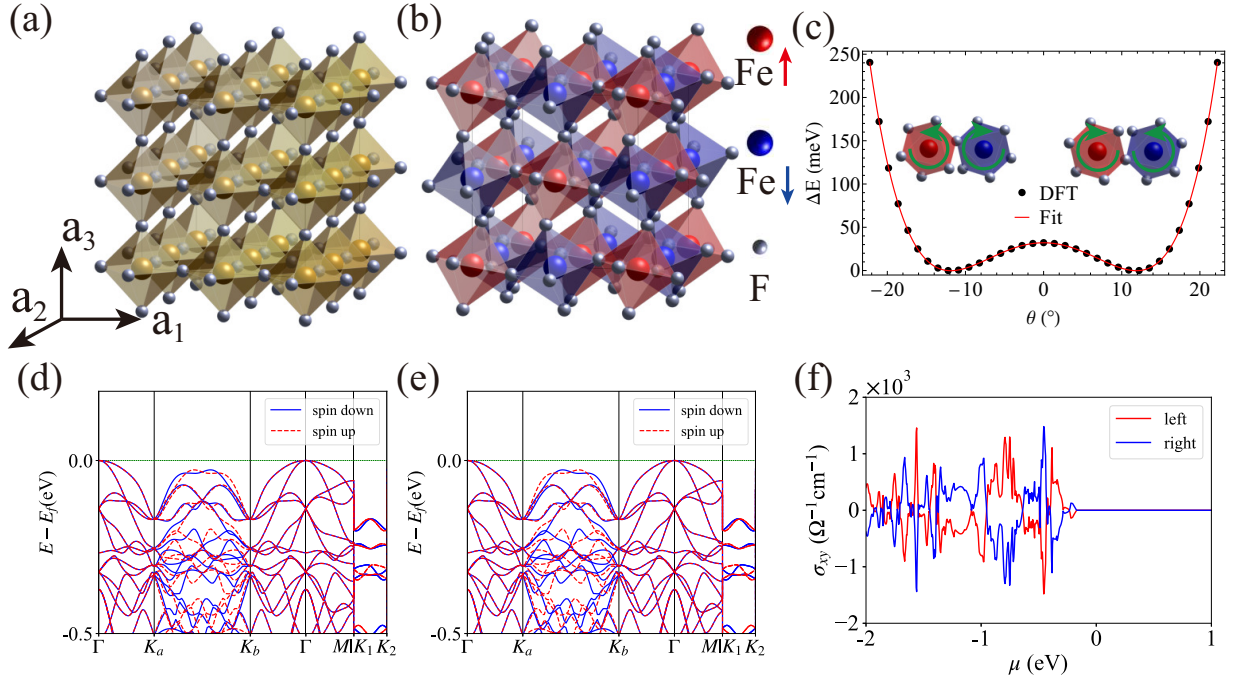


FIG. S7. Multiferroic switching in the bulk *g*-wave altermagnet FeF₃. (a) The parent phase *Pm* $\bar{3}m$ with ideal octahedra. The antiferroaxial transition involves counter-rotations along the (111) direction (b). (c) Total energy profile as a function of the rotation angle θ , showing a double-well potential. The effective Landau free energy per unit cell is well fit to $\mathcal{F}_{\text{eff}}(\theta) = 32.1 - 0.446\theta^2 + 1.45 \times 10^{-3}\theta^4$, where \mathcal{F}_{eff} is in meV per unit cell and θ is in degrees. (d) Band structure for the equilibrium state $\theta = 12^\circ$. (e) Band structure for the reversed state $\theta = -12^\circ$, showing inverted spin splitting. (f) Anomalous Hall conductivity (AHC) as a function of chemical potential μ for $\theta = \pm 12^\circ$, demonstrating the sign reversal of the transport signature.

X_3^+ and $\mathbf{N} \sim X_1^+$. Their bilinear combination transforms as

$$G_{110}\mathbf{N} \sim X_3^+ \otimes X_1^+ = \Gamma_5^+(E_g), \quad (\text{S-51})$$

which couples to the E_g channel of the rank $\ell = 2$ magnetic multipole, indicating a *d*-wave altermagnetic state. Upon condensation, G_{110} lowers the crystallographic symmetry to *I4₂/ncm*, and the Néel order further reduces it to the space group *Pccn* (point group *mmm*), in which the Néel order transforms as Γ_3^+ , consistent with the d_{xy} -wave altermagnetic spin splitting shown in Fig. S10(c).

Computational details: We used $U = 6$ eV for atom Ni and a $9 \times 9 \times 4$ k mesh (cutoff 550 eV).

[1] D. M. Hatch and H. T. Stokes, *Isotropy subgroups of the 230 crystallographic space groups* (World Scientific, 1989).
[2] M. I. Aroyo, A. Kirov, C. Capillas, J. M. Perez-Mato, and H. Wondratschek, *Acta Crystallographica Section A* **62**, 115 (2006).
[3] S. Froyen and W. A. Harrison, *Phys. Rev. B* **20**, 2420 (1979).
[4] H. T. Stokes, S. v. Orden, and B. J. Campbell, *Applied Crystallography* **49**, 1849 (2016).
[5] D. M. Hatch and H. T. Stokes, *Applied Crystallography* **36**, 951 (2003).
[6] G. Kresse and J. Furthmüller, *Phys. Rev. B* **54**, 11169 (1996).
[7] J. P. Perdew, K. Burke, and M. Ernzerhof, *Phys. Rev. Lett.* **77**, 3865 (1996).
[8] A. A. Mostofi, J. R. Yates, Y.-S. Lee, I. Souza, D. Vanderbilt, and N. Marzari, *Comput Phys Commun* **178**, 685 (2008).
[9] J. Wang, X. Yang, Z. Yang, J. Lu, P. Ho, W. Wang, Y. S. Ang, Z. Cheng, and S. Fang, *Advanced Functional Materials* **n/a**, 2505145 (2025).
[10] J. Sødequist and T. Olsen, *Applied Physics Letters* **124**, 182409 (2024).
[11] K. S. Knight, D. D. Khalyavin, P. Manuel, C. L. Bull, and P. McIntyre, *Journal of Alloys and Compounds* **842**, 155935 (2020).
[12] C. Autret, C. Martin, M. Hervieu, R. Retoux, B. Raveau, G. André, and F. Bourée, *Journal of Solid State Chemistry* **177**, 2044 (2004).

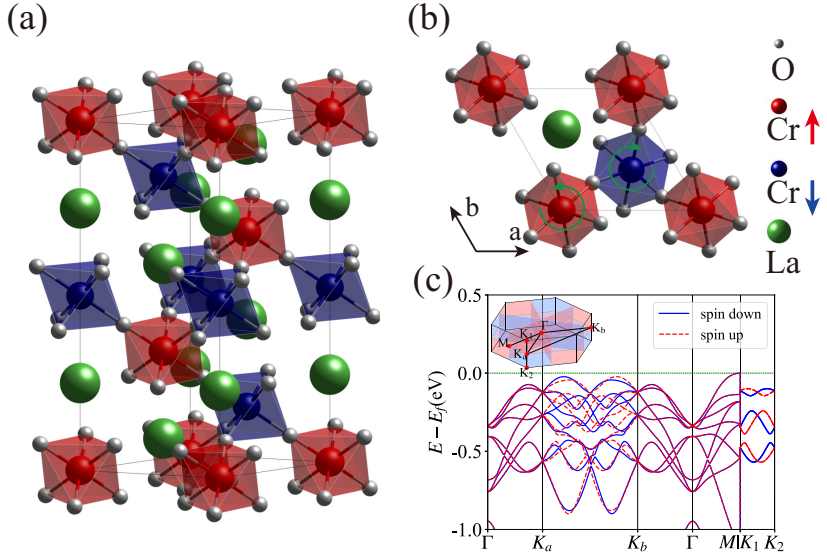


FIG. S8. The structure, antiferroaxial distortion and band structure of LaCrO_3 . (a) Crystal structure of LaCrO_3 (parent space group $Pm\bar{3}m$). (b) The antiferroaxial distortion corresponding to the R_4^+ rotation mode of the $\text{Cr}-\text{O}_6$ octahedra (parent group $Pm\bar{3}m$). (c) Band structure exhibiting bulk g -wave altermagnetic spin splitting.

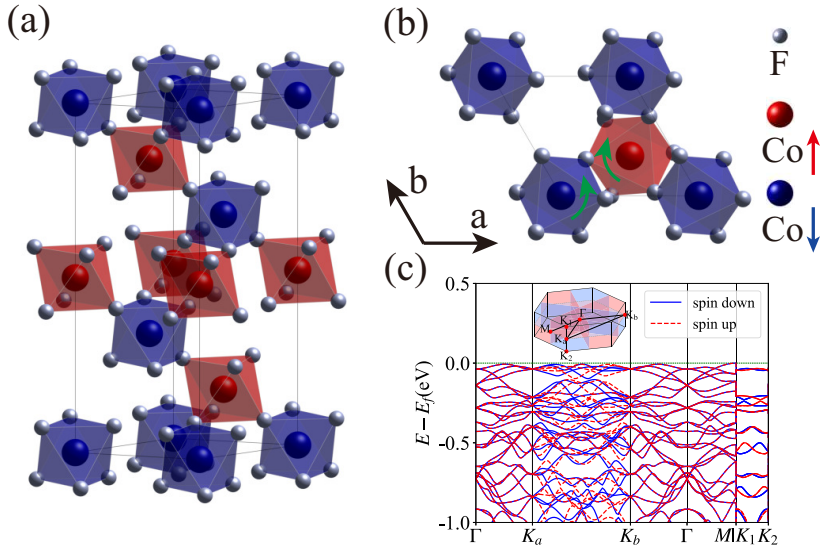


FIG. S9. The structure, antiferroaxial distortion and band structure of CoF_3 . (a) Crystal structure of CoF_3 (parent space group $Pm\bar{3}m$). (b) The antiferroaxial distortion corresponding to the R_4^+ rotation mode of the $\text{Co}-\text{F}_6$ octahedra. (c) Band structure exhibiting bulk g -wave altermagnetic spin splitting.

- [13] S. Lee, S. Torii, Y. Ishikawa, M. Yonemura, T. Moyoshi, and T. Kamiyama, *Physica B: Condensed Matter The 11th International Conference on Neutron Scattering (ICNS 2017)*, **551**, 94 (2018).
- [14] S. Mattsson and B. Paulus, *Journal of Computational Chemistry* **40**, 1190 (2019).
- [15] X. Wang, J. R. Yates, I. Souza, and D. Vanderbilt, *Physical Review B* **74**, 195118 (2006).
- [16] Y. Yao, L. Kleinman, A. H. MacDonald, J. Sinova, T. Jungwirth, D.-s. Wang, E. Wang, and Q. Niu, *Physical Review Letters* **92**, 037204 (2004).
- [17] J.-S. Zhou, J. A. Alonso, A. Muoñz, M. T. Fernández-Díaz, and J. B. Goodenough, *Physical Review Letters* **106**, 057201 (2011).
- [18] J. Rodriguez-Carvajal, M. T. Fernandez-Díaz, and J. L. Martínez, *Journal of Physics: Condensed Matter* **3**, 3215 (1991).

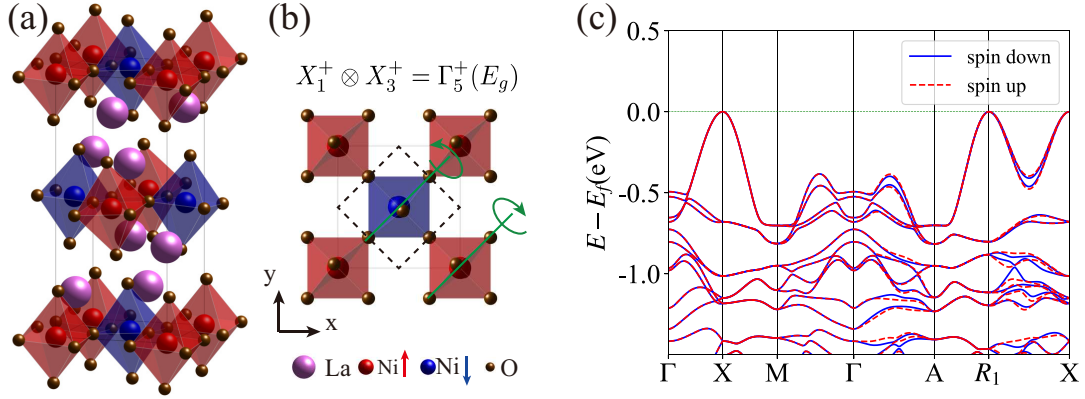


FIG. S10. The structure, antiferroaxial distortion and band structure of La_2NiO_4 . (a) Crystal structure of La_2NiO_4 (parent space group $I4/mmm$). (b) Antiferroaxial distortion associated with the X -point mode $G_{110} \sim X_3^+$, involving rotations of NiO_6 octahedra about in-plane diagonal axes. (c) Band structure exhibiting d -wave altermagnetic spin splitting in the ordered phase.